Department of Physics and Astronomy

Heidelberg University

Diploma thesis
in Physics
submitted by
Moritz Simon Maria Kiehn
born in Menden (Sauerland)
2012

Track Fitting with Broken Lines for the MU3E Experiment

This diploma thesis has been carried out by

Moritz Simon Maria Kiehn

at the

Institute of Physics

under the supervision of

Prof. Dr. André Schöning

Zusammenfassung

Das Standardmodell der Teilchenphysik ist erstaunlich erfolgreich in der Beschreibung der Eigenschaften der Elementarteilchen und ihrer Interaktionen. Trotzdem gibt es noch viele offene Fragen und mehrere Modelle für Physik jenseits des Standardmodells. Das geplante MU3E Experiment soll nach dem Lepton Flavor verletzenden Zerfall $\mu \to eee$ suchen. Dieser Zerfall ist im Standard Modell stark unterdrückt und eine Beobachtung wäre ein klarer Hinweis auf neue Physik.

Das geplante MU3E Elektronenspektrometer besteht aus vier zylindrischen Lagen dünner Silizium Pixelsensoren im Feld eines Solenoidmagneten. Aufgrund des geringen Elektronenimpulses spielt Vielfachstreuung eine große Rolle und dominiert die Messungenauigkeit. In dieser Arbeit wird ein neuer Spurrekonstruktionsalgorithmus basierend auf "broken lines" untersucht, der die Winkel der Vielfachstreuung explizit berücksichtigt. Das Rekonstruktionsverhalten wurde mit dem eines konventionellen "fast helix fit" durch Simulationen verglichen.

Der "broken lines" Algorithmus erreicht eine bis zu 50 % bessere Spurauflösung, insbesondere in der Position, und eine korrekte Beschreibung der Fehler. Diese Ergebnisse bestätigen, dass eine Implementierung eines auf "broken lines" basierenden Algorithmus die Spurrekonstruktion deutlich verbessert und unverzichtbar ist, um die geplante Sensitivität eines Verzweigungsverhältnisses von $BR(\mu \to eee) < 1 \times 10^{-16}$ zu erreichen.

Abstract

The Standard Model of elementary particle physics has been surprisingly successful in describing the properties of particles and their interactions. However, many open questions still exist, and there are a number of models for physics beyond the Standard Model. The MU3E project is a proposed experiment to search for the lepton flavor changing decay $\mu \to eee$. This decay is highly suppressed in the SM, thus an observation would be a clear sign of new physics.

The MU3E detector is an electron spectrometer built with four cylindrical layers of thin silicon pixel sensors in a solenoidal magnetic field. Due to the low momentum of the electrons, multiple scattering is significant and dominates the measurement uncertainties. I investigated a new track fitting algorithm based on broken lines, that directly takes scattering angles into account. Fit performance was compared to a conventional fast helix fit on the basis of simulations.

The broken lines fit reaches an up to 50 % higher parameter resolution, with the most significant improvement in the track positions. More important, it provides correct error estimates. These results confirm that an implementation of a broken lines fit is greatly beneficial for track reconstruction and indispensable to reach the proposed branching ratio sensitivity of $BR(\mu \to eee) < 1 \times 10^{-16}$.

„Remember: KING KONG Died For Your Sins"

— Malaclypse the Younger
in: *Principia Discordia*

Contents

List of Figures

Chapter 1

Introduction

The Standard Model of elementary particle physics (SM) has been surprisingly successful in describing the properties of particles and their interactions in a unified fashion. However, many open questions still exist, e.g. the problem of the large mass hierarchy and small neutrino masses or the missing unification with gravity, for which the SM does not give a satisfactory answer. Many theories have been proposed to solve these problems which in turn would give rise to new phenomena that are not yet described by the SM. Since none of them have been observed thus far, these possible phenomena, or new physics in general, necessarily need to come into play only at high mass scales that have not been accessible yet.

The on-going search for new physics is pursued at different frontiers. The most prominent one is the energy frontier that is investigated at high energy particle colliders e.g. at the Large Hadron Collider. At very high energies, signatures for the production of new particles or the appearance of new processes are searched for directly.

A second frontier is the intensity frontier. Instead of searching directly for new physics phenomena, very precise measurements of known quantities are performed at lower energies to look for small deviations from the expected SM values. This comprises the search for very rare or forbidden[1] decays, precision measurements of particle properties such as the muon magnetic moment and its gyromagnetic ratio or (heavy) flavor spectroscopy at specialized storage rings.

Due to their quantum nature, processes at high mass scale also have an impact on low energy processes. An indirect search for new physics is possible already at lower energies. To achieve the required high precision,

[1] In the Standard Model.

often at the parts-per-billion level or below, high statistics and consequently high intensities are necessary.

The MU3E experiment is a recently proposed precision experiment [Sch+12] to search for the lepton flavor violating muon decay $\mu^+ \to e^+e^+e^-$ with a planned branching ratio sensitivity of 1×10^{-16} at 90 % confidence level. Depending on the theory, this branching ratio sensitivity translates to a sensitivity in mass-scale of up to 1×10^4 TeV, which is beyond the reach of current direct searches.

To measure this rare decay, a continuous high-intensity muon beam is stopped in an extended target. The decay products, i.e. electrons with a momentum bound by half of the muon mass, are measured in a magnetic spectrometer with four cylindrical detector layers built from thin silicon pixel sensors. Due to the low momentum of the electrons, the uncertainty of the track reconstruction is dominated by the effects from multiple Coulomb scattering. Special care needs to be taken to handle the resulting correlations and additional uncertainties in the track reconstruction.

Traditionally, this has been done by treating multiple scattering as an additional source of random errors in a global fit. This requires the calculation and inversion of the measurement covariance matrix induced by multiple scattering. Current particle physics experiments, e.g. ATLAS or CMS, usually employ iterative track fitting procedures based on the Kálmán-filter [Fru87]. In these methods, multiple scattering is treated as additional random noise at each iteration step. The broken lines fit [Blo06] is a novel approach that takes the possible scattering angles in the trajectory into account explicitly while allowing a non-iterative solution. In this thesis, I will investigate the suitability and the performance of this novel track fitting approach in the context of the MU3E project.

The first part of the thesis in chapter 2 is concerned with a theoretical discussion of the lepton flavor violating muon decay $\mu \to eee$ in the SM and in new physics models. This discourse is followed by a description of the experimental design of the proposed MU3E experiment and its key features in chapter 3. Chapter 4 derives the track model and associated techniques that form the basis of the subsequent discussion on track fitting in chapter 5. Two different track fitting algorithms, a fast helix fit and the broken lines fit, are presented and discussed in detail. The performance of these different algorithms in the context of the MU3E experiment is analyzed in chapter 6 and the thesis concludes with a summary and an outlook into possible future developments in chapter 7.

Chapter 2

Theoretical Background

In the original standard model (SM) formulation the lepton flavor, a quantum number attributed to elementary particles called leptons, should be a conserved quantity. It has already been verified that this is not the case for neutral leptons, the neutrinos, but no lepton flavor violation has been found for interactions of charged leptons. Yet, many new physics models predict lepton flavor violation also in systems involving charged leptons. In this chapter I will introduce the SM and subsequently concentrate on lepton flavor violation in rare muon decays.

2.1 The Standard Model

The SM is a quantum field theory that describes the known elementary particles and their interactions. It contains twelve elementary matter particles, their respective antiparticles and six particles that mediate the interactions. The SM describes only three of the four known fundamental interactions: the strong, the weak and the electro-magnetic interactions. Gravitational effects are negligible at the energy scales of particle interactions and gravitation is not part of the SM.

Matter particles in the SM are defined by their mass and their quantum numbers: spin, electric charge (usually given in units of the elementary charge e), weak hypercharge, color charge and flavor quantum number. All the matter particles are fermions with spin 1/2 whereas all the gauge interactions are mediated by bosons with spin 1. The additional Higgs particle is a scalar boson with spin 0. It is somewhat separated because it is neither a matter particle nor does it mediate a gauge interaction. Figure 2.1 shows an overview over all the particles.

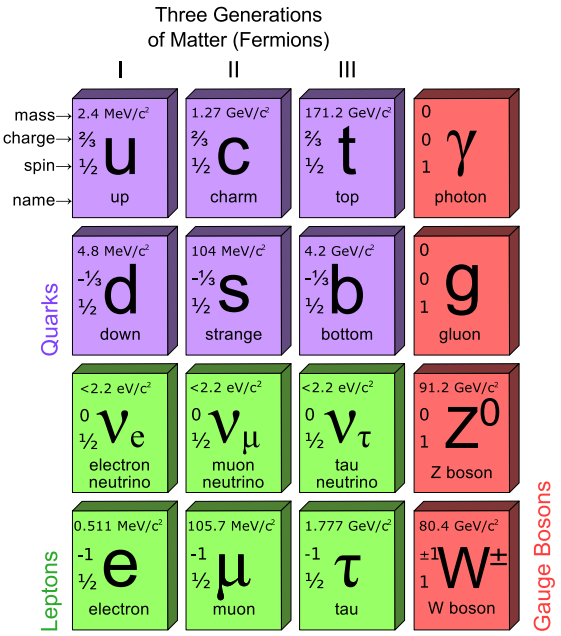

Figure 2.1: The experimentally verified Standard Model particles and their measured properties. The Higgs boson is missing because it has not been found yet. [Wik]

2.1.1 Fermions

Fermions can be divided into two groups of six particles each, quarks and leptons, based on their quantum numbers. Both groups can be arranged into three generations or families ordered by increasing mass (see e.g. [Per00]).

Quarks are the only fermions that have a color charge and thus are the only elementary particles that interact strongly. The up-type quarks up, charm and top have a charge of $2/3$ and the down-type quarks down, strange and bottom have a charge of $-1/3$. One up-type and one down-type quark together form one quark generation in the way shown in Figure 2.1. They also interact electro-magnetically and weakly. Quarks do not exists as free particles in nature. They are only found in so-called hadrons, strongly-bound, color-neutral states of multiple quarks, a property unique to quarks known as *confinement*.

Leptons do not have a color charge and cannot interact strongly. The charged leptons are the electron (e), the muon (μ) and the tau (τ). They all have a charge of -1 and can interact electro-magnetically and weakly.

For each charged lepton there is a corresponding neutral lepton called a neutrino, e.g. the electron-neutrino (ν_e) for the electron. Together they form one lepton generation, which is identified by a quantum number called lepton flavor. For example, the electron and the electron-neutrino both have a flavor number of $l_e = 1$. In contrast to all the other fermions, neutrinos are massless in the SM.

However, with the experimental discovery of neutrino oscillations it became clear that neutrinos must have a small, but non-vanishing mass [Fuk+98; Ahm+01; Egu+03]. An extension of the SM, hereafter referred to as νSM, accounts for this finding and introduces the Pontecorvo-Maki-Nakagawa-Sakata matrix (PMNS) [MNS62] that relates the neutrino eigenstates of the weak interaction with their mass eigenstates.

For every matter particle, there exists a corresponding anti-matter particle with identical properties, but opposite electrical charge, color charge or flavour quantum number. For example the positron is the anti-particle of the electron whereas the anti-muon is the anti-particle of the muon.

2.1.2 Interactions

All interactions in the SM are mediated trough the exchange of so-called gauge bosons. The strength and the range of each interaction is determined by the mass of its gauge boson(s) and its coupling to the fermions given by a coupling constant that is usually denoted α. All gauge bosons in the SM have spin 1.

The gauge boson of the electro-magnetic (EM) interaction is the photon (γ). It couples to all electrically charged particles and is massless. As a result, the EM interaction has an infinite range. The weak interaction is mediated by three gauge bosons: two W bosons with a mass of about 80.4 GeV and the Z boson with a mass of about 91.2 GeV [Nak+10]. The W bosons have an electric charge of ± 1 whilst the Z boson is a neutral particle. The high mass of the gauge bosons limits the range of the interaction and renders it the weakest interaction in the SM.[1] The gauge boson of Quantum Chromo Dynamics (QCD), the theory of strong interactions, is the massless gluon. It is electrically neutral but, in contrast to the other gauge bosons, it has a color charge. This allows the interaction of gluons with themselves and makes the strong interaction a short-range interaction. This effect is

[1] This is only true for energy scales lower than the mass of the W or Z bosons.

different from the short-range weak interaction, where the limited range is due to the high mass of the force carrier.

The electro-magnetic and the weak interactions can be unified into a single interaction — the electro-weak interaction — with four massless gauge bosons. The process that breaks the single electro-weak interaction into two and generates massive gauge bosons for the weak interaction is called electro-weak symmetry breaking. In the SM this is done using the so-called Higgs-mechanism which introduces an additional scalar, neutral particle: the Higgs boson [Hig64; EB64; GHK64]. The Higgs boson is the only particle in the SM that has not been experimentally detected. The search for it, e.g. at the Large Hadron Collider (LHC), is on-going [Aad+11a; CMS11].

2.1.3 Symmetries and Conserved Quantities

Every differentiable symmetry of the action of a physical system is associated with a corresponding conservation law. The former statement is a formulation of the famous Noether theorem [Noe18], which, applied to the standard model, results amongst others in the conservation of the flavor quantum number for the strong and electro-magnetic interaction.

One example for a non-conserved quantity is the quark flavor in weak processes. The weakly interacting quark states are not identical to the quark states that interact strongly or electro-magnetically. Instead, the weak quark eigenstates are mixtures of the strong eigenstates with a mixing given by the Cabibbo-Kobayashi-Maskawa matrix (CKM). This breaks the underlying symmetries and makes the quark flavor a non-conserved quantity.

In the original SM formulation lepton flavor would be a conserved quantity, i.e. lepton flavor changing processes are forbidden. However, this is not the case anymore in the νSM where only the more relaxed condition of lepton number conservation (irrespective of the generation) is valid. Here, the mixing of the neutrino mass eigenstates via the PMNS matrix breaks the underlying symmetries and allows for lepton flavor violation. As a result, measuring these lepton flavor non-conserving processes can give, courtesy of the Noether-theorem, insight into the fundamental symmetries of nature.

2.1.4 Limitations and New Physics

The SM and its extension νSM has been very successful in describing all known particles and their interactions over a wide range of energy scales. However, a number of open questions and theoretical problems exist.

A first example is gravity. Although it is the sole important interaction on astronomical length scales, it does not play any role on the scale of particle interactions. Second, the matter content in the νSM constitutes only about 5 % of the known energy content of the universe. The remaining 95 % are dark matter and dark energy for which no theoretical explanation has been found so far. Third, the particles observed so far show a very unique mass hierarchy. The process by which the neutrinos acquire a non-vanishing mass is unknown and the fact that its values are many orders of magnitudes lower than any other particle is quite startling. In addition, the resulting mixing of leptons is fundamentally different from the flavor mixing in the quark-sector. The CKM matrix is nearly diagonal whereas the PMNS matrix is tribimaximal. This also posesses a problem for the question of grand unification. The SM describes all the interactions within a common framework but they are still distinct and only the weak and the electro-magnetic interactions have been successfully unified.

Although this list of open questions is not fully comprehensive, it is clear that the SM or the νSM cannot be the *unified theory of everything* and that a more complete explanation is needed. A multitude of suggested theories exists with varying predictions for possible new phenomena.

2.2 Lepton Flavor Violation in Charged Lepton Decays

2.2.1 In the Standard Model

The original SM contains no lepton flavor violating processes and the neutrino weak eigenstates are the same as the mass eigenstates. The νSM allows lepton flavor violation but it has only been observed in the neutral lepton sector via neutrino oscillations. While charged lepton flavor violation does not exists on tree-level even in the νSM, the mixing of neutrinos can produce charged lepton flavor violation on the loop-level.

One possible lepton flavor violating decay is the three electron decay of the muon ($\mu \to eee$) shown in Figure 2.2. Although allowed, it is greatly

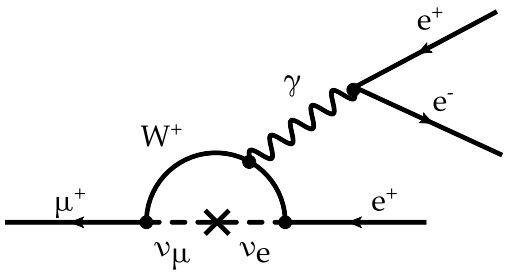

Figure 2.2: The Standard Model loop-level diagram for the decay $\mu \rightarrow$ eee.

suppressed by the fourth power of the high mass ratio ($\sim \Delta m_\nu / m_W$) of the particles running in the loop. The W boson has a mass of about 80.4 GeV and the mass of the neutrinos has an upper bound of about 2.2 eV [Nak+10]. Therefore, the branching ratio for the decay $\mu \rightarrow$ eee in the Standard Model is $< 10^{-50}$.

Another possible decay is the neutrino-less radiative decay of the muon ($\mu \rightarrow e\gamma$). It is very similar to the three electron decay described above. The radiated γ in Figure 2.2 is now a real particle instead of a virtual one that splits into an electron-positron pair. The branching ratio differs only in the additional factor of α_{em} from the pair production vertex and is equally suppressed.

The very low expected branching ratios make these decays practically unmeasurable. Any measurement of the aforementioned decay would therefore be a clear indicator for new physics.

2.2.2 New Physics Models

Many theories for physics beyond the Standard Model include additional flavor violating processes in the charged lepton sector, e.g. the decay $\mu \rightarrow$ eee. The expected branching ratio for those decays depends on the model parameters and is constrained both by the current experimental limits for the decay itself, e.g. BR($\mu \rightarrow$ eee) $< 1 \times 10^{-12}$ [Bel+88], as well as by other measurements in the charged lepton sector, e.g. limits on $\mu \rightarrow e\gamma$ and $\mu \rightarrow$ e conversion.

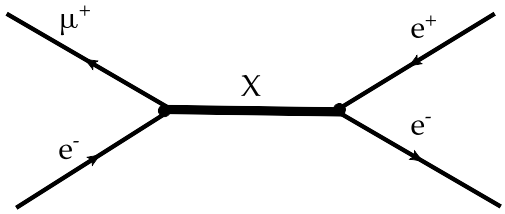

Figure 2.3: A generic tree level diagram for the decay $\mu \to eee$ in a physics model beyond the Standard Model. The new heavy intermediate particle could be an additional Higgs boson or a Z'.

On Tree-Level

One way to introduce additional lepton flavor violating processes is by adding new heavy particles with couplings to both electrons and muons already at the tree-level. This would lead to contributions from diagrams like the one shown in Figure 2.3. These contributions occur e.g. for models with extra dimensions [CN05] or for models with an extended Higgs sector [Bla+07; KOS03]. For these models the high suppression of the lepton flavor violating decays is due to the high mass of the new intermediates.

On Loop-Level

The other possibility is to introduce new lepton flavor violating physics only at the loop level [HK85]. One possible family of models are the supersymmetric (SUSY) extensions of the Standard Model. In these models, each SM particle has an additional partner particle, its superpartner, which has opposing spin statistics. The superpartners of fermions are bosons and vice versa. The symmetry that generates these additional particles has to be broken to allow the supersymmetric particles to have a mass that is different from the normal particles. This is necessary, since supersymmetric particles have not been observed so far (e.g. [Aad+11c; Aad+11b]) and consequently their production needs to suppressed by their high mass.

The additional contributions, e.g. for the decay $\mu \to eee$, are given e.g. by the diagram shown in Figure 2.4. This diagram is very similar to the SM one shown in Figure 2.2. Instead of a W boson and neutrinos, new supersymmetric particles are running in the loop. The lepton flavor violation is produced via slepton mixing instead of neutrino mixing. The supersym-

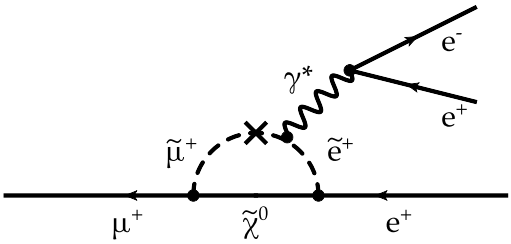

Figure 2.4: A possible loop level diagram for the decay $\mu \to eee$ in a supersymmetric extension of the Standard Model. The mixing particles in the loop are sleptons and the additional neutral particle is a neutralino.

metric particles can have similar mass which reduces the suppression due to the mass difference.

For models that prefer loop-level diagrams, the two different muon decay modes $\mu \to e\gamma$ and $\mu \to eee$ are essentially generated via the same loop-level diagram. The only difference is whether the emitted γ, e.g. in Figure 2.4, is real or virtual. It is virtual for the three electron decay with an additional vertex to create the electron-positron pair. Consequently, the expected branching ratio for the three electron decay is suppressed by a factor of α_{em} with respect to the neutrino-less radiative decay $\mu \to e\gamma$.

2.3 An Effective Theory for the Decay $\mu \to eee$

Directly comparing all the different new physics models and their predictions for the lepton flavor violating charged decays is not a sensible choice. The number of parameters and their possible combinations is beyond measure. However, the possible sensitivity in mass scale and the discriminating power for different new physics models can be estimated by using an effective theory. This also allows a comparison of the different decay modes. The following simplified Lagrangian is used to describe the three electron decay in different new physics models [KO01].

$$L = \frac{m_\mu}{(1+\kappa)\Lambda^2}\overline{\mu_R}\sigma^{\mu\nu}e_L F_{\mu\nu} + \frac{\kappa}{(1+\kappa)\Lambda^2}(\overline{\mu_L}\gamma^\mu e_L)(\overline{e_L}\gamma_\mu e_L) \qquad (2.1)$$

The first term describes a contribution from loop-level diagrams (dipole coupling). The second term is a contact interaction with left-left vector

coupling and an example for a possible tree-level contribution. This is one possible term from a more general expression for the contact interaction. The effective theory only has two parameters: Λ is the effective mass scale[2] of the theory and κ is the amplitude ratio between the two terms. The loop-level interactions dominate in the low-κ region and the tree-level interactions dominate in the high-κ region.

Employing a four fermion contact interaction to approximate the contribution from tree-level diagrams, similar to Fermi's theory for weak interactions, is well motivated by the expected energy scales. The energy of the decay is the fixed to the muon mass $m_\mu \approx 106\,\text{MeV}$. The new physics scale must be beyond the electroweak scale of about 100 GeV; orders of magnitude above the scale of the decay.

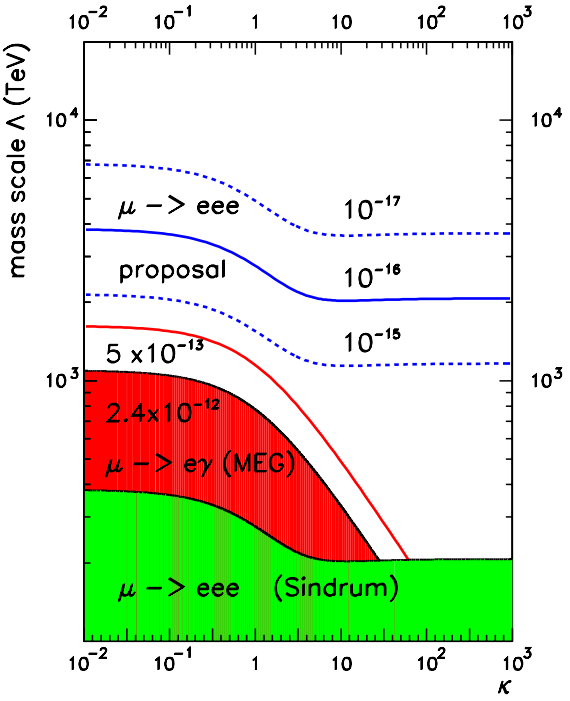

Figure 2.5: The expected branching ratios and the current experimental limits for the decays $\mu \to eee$ and $\mu \to e\gamma$ in an effective theory. Λ is the effective massscale and κ describes the mixing between the contact interaction term and the dipole coupling term. [Ber11]

Figure 2.5 shows lines of constant branching ratio as functions of the two parameters of the effective theory. The blue lines are for the decay

[2]The scale at which new physics exists assuming that all the couplings are one.

$\mu \to eee$. The solid areas are parameter spaces already excluded by previous measurements. The additional red line indicates the expected sensitivity of the MEG experiment [Ada+11b]. The MEG experiment is searching for the decay $\mu \to e\gamma$ and is currently running at the Paul Scherrer Institute.

For a given mass scale the value of κ distinguishes between different types of theories. To constrain the mass scale in the low-κ regime, the sensitivity for the decay $\mu \to eee$ needs to be about two orders of magnitude higher than for the decay $\mu \to e\gamma$. Here, the SUSY-like models dominate and the three electron decay is suppressed by the additional photon vertex. This is different for the high-κ regime. Models with tree-level contributions dominate and the three electron decay is preferred.

2.4 Comparison and Expected Sensitivity

As seen in Figure 2.5, the accessible effective mass range is about 10^3 TeV to 10^4 TeV. Depending on the model, this equates to a sensitivity to mass scales far beyond current direct searches e.g. at the LHC. Therefore, a search for the lepton flavor violating decay $\mu \to eee$ is complimentary to both current precision experiments in other muon decay channels and to direct new physics searches at high energies.

Chapter 3

The MU3E Experiment

The MU3E project is a proposed experiment to search for the lepton flavor violating decay $\mu^+ \to e^+e^+e^-$ with a projected branching ratio sensitivity of 10^{-16} at the 90 % confidence limit [Sch+12]. This would be an increase in sensitivity of nearly four orders of magnitude compared to the previous limit of BR($\mu^+ \to e^+e^+e^-$) < 1.0×10^{-12} from the SINDRUM collaboration. This requires a high number of measured muon decays and consequently, a very fast detector for the decay products. To reach this level of sensitivity it is necessary to have a relative background suppression better than the branching ratio sensitivity. This requires a very high momentum, vertex and time resolution. The detector for the MU3E experiment would be made of thin active silicon pixel sensors and include a scintillating fiber hodoscope built around an extended target to stop muons. The detector shall be installed at a high-intensity muon beamline at the Paul Scherrer Institute (PSI) in Switzerland.

3.1 Current Experimental Situation

3.1.1 The SINDRUM experiment

The current limit on the $\mu^+ \to e^+e^+e^-$ branching ratio was set by the SINDRUM experiment. It was running at running at the Paul Scherrer Institute in Villingen, Switzerland (PSI) from 1983-86. They found no signal event for the decay $\mu^+ \to e^+e^+e^-$ and set the limit BR($\mu^+ \to e^+e^+e^-$) < 1×10^{-12} at 90 % confidence limit [Bel+88].

The experiment used a low energy surface muon DC beam with a nearly monochromatic energy of about 28 MeV/c. The muons were stopped in

a hollow double-cone target. The decay electrons from the muon decays were measured using five layers of multiwire proportional chambers for the tracking measurement and an additional fibre hodoscope for triggering and timing measurements. The detector was positioned inside a solenoidal magnetic field of 0.33 T.

3.1.2 The MEG experiment

The MEG experiment is running at the PSI since 2008 and searching for the lepton flavor violating decay $\mu^+ \to e^+\gamma$. The current limit for the branching ratio is $BR(\mu \to e\gamma) < 2.4 \times 10^{-12}$ [Ada+11a].

The experiment uses a low energy surface muon DC beam[1] but the beam is stopped on a small thin target. Drift chambers are used to measure the single electron track and a liquid xenon calorimeter to detect the photon.

The main limitation comes from the accidental coincidence of high energy photons and single positrons from regular Michel decays. The maximum sensitivity is estimated to be on the order of a few 10^{-13}. This requires a branching ratio sensitivity of 1×10^{-15} for the decay $\mu \to eee$ to be competitive in the case of dominating dipole couplings, see section 2.2.

3.2 Muon Decays

Before explaining the proposed experimental realization of this project, the signal decay and its possible backgrounds will be discussed in detail.

Anti-muons have a very long lifetime of 2.2 µs and due to the low mass and charge conservation can only decay into positrons, neutrinos and photons. The dominant decay mode is the lepton flavor conserving decay $\mu^+ \to e^+\nu_e\overline{\nu}_\mu$ with a branching ratio of almost a 100 % [Nak+10]. The only measurable decay product is a single positron whose energy spectrum is described by the so-called Michel spectrum.[2] The parameter of the electron spectrum have been most precisely measured by the TWIST collaboration [Bay+11]. Other known lepton conserving decays are decays with additional photons or electrons, e.g. $\mu^+ \to e^+\gamma\nu_e\overline{\nu}_\mu$ with a branching ratio[3] of 10^{-2} and $\mu^+ \to e^+e^+e^-\,\nu_e\overline{\nu}_\mu$ with a branching ratio of 3.4×10^{-5}

[1] The muon energy is the same as for the SINDRUM experiment

[2] As a result, the decay itself is called the Michel decay.

[3] For photon energies above ~ 10 MeV.

[Nak+10]. Assuming that the muon is at rest in the lab frame, the energy of the decay products is limited to half the muon mass, i.e. $\sim 53\,\mathrm{MeV}$.

Possible signal decays are very rare, but they have a distinct signature compared to the dominant decay modes. However, due to low signal rate it is very important to suppress possible background from accidental coincidences and mismeasured tracks. This is discussed in the following sections.

3.2.1 Signal Decay and Topology

The signal decay $\mu^+ \to e^+e^+e^-$ is defined by its final state: two positrons and one electron without any additional neutrinos. All the tracks originating from the decay share a single common vertex and they are coincident in time. The invariant mass of the three tracks, measured at the vertex position, is identical to the muon mass.

$$m_\mu^2\, c^4 = \left(\sum_{i=1}^{3} P_i \right)^2 \tag{3.1}$$

Assuming that the muon is stopped in the target, i.e. that it is at rest in the laboratory frame, the vectorial sum of the momenta must vanish.

$$\left| \boldsymbol{p}_{abs} \right| = \left| \sum_{i=1}^{3} \boldsymbol{p}_i \right| = 0 \tag{3.2}$$

For three momentum vectors to fulfill (3.2) they all have to lie in the same decay plane. A possible decay topology, projected to the transverse plane, is illustrated in Figure 3.1. The blue tracks correspond to the decay electrons and the different curvatures represent the different transverse momenta.

3.2.2 Backgrounds

As shown in section 2.2 the decay $\mu^+ \to e^+e^+e^-$ has no irreducible background. Any background to the signal therefore comes from processes that generate fake signals. These reducible backgrounds can be roughly separated into two groups: accidental and internal conversion background.

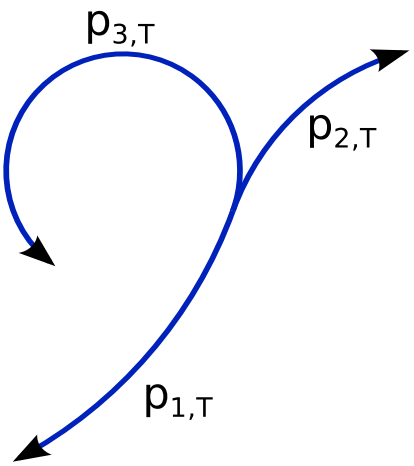

Figure 3.1: The topology of the signal decay in the transverse plane.

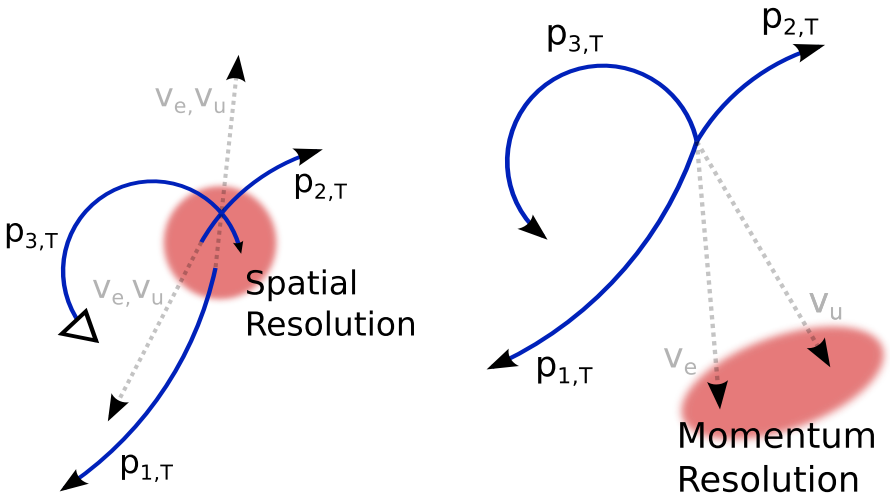

(a) Accidental Background (b) Internal Background

Figure 3.2: The topologies of possible backgrounds in the transverse plane. (a) originates from the accidental coincident of independent Michel-decays. (b) comes from internal conversion decays with a very small missing energy.

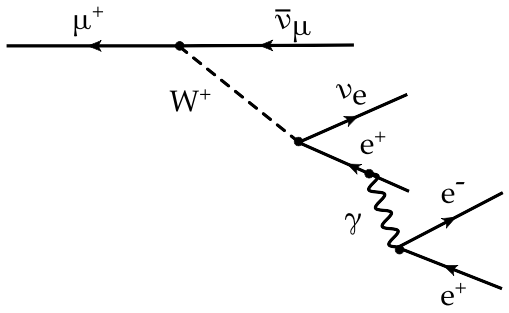

Figure 3.3: The Feynman diagram for the internal conversion decay $\mu^+ \to e^+e^+e^- \nu_e\overline{\nu}_\mu$.

Accidental Background

Accidental background originates from the random coincidence in phase-space of three electron tracks that originate from independent processes. One example of such a combination is shown in figure 3.2a. Here, two positron tracks come from two independent Michel decays and the electron track comes from a positron track with a mismeasured charge, e.g. due to a recurling track. A similar situation can ensue from the overlay of an electron-positron pair created by photon conversion or Bhabha-scattering and an additional Michel positron.

In contrast to the signal, accidental background is not coincident in time or space and the total momentum does not fulfill the requirements given by (3.1) and (3.2). To suppress these kinds of backgrounds a high vertex and time resolution is needed.

Internal Conversion Background

The other type of background comes from internal conversion decays. These are radiative decays where the radiated photon immediately converts to an electron-positron pair as illustrated in Figure 3.3. The resulting decay $\mu^+ \to e^+e^+e^- \nu_e\overline{\nu}_\mu$ has a branching ratio of BR = 3.4×10^{-5} [Nak+10]. In some parts of the phase-space the measurable final state is nearly identical to the signal. There are three electron tracks, one of which has a negative charge, they share a common vertex and they are coincident in time. This arangement is indistinguishable from the signal decay. The topology of this background is shown in Figure 3.2b.

However, there are two additional neutrinos in the final state and the three electron tracks do not fulfill the required energy and momentum

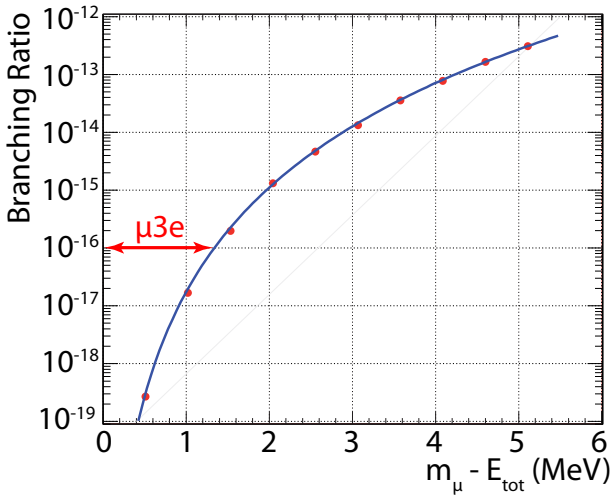

Figure 3.4: The effective branching ratio for the internal conversion decay $\mu^+ \to e^+e^+e^- \nu_e\overline{\nu}_\mu$ as a function of the energy carried by the neutrinos. The red arrow indicates the planned branching ratio sensitivity for the signal decay $\mu^+ \to e^+e^+e^-$. This plot is adapted from Djilkibaev and Konoplich [DK09].

relations defined in (3.1) and (3.2). The phase-space region, for which this background decay is indistinguishable from the signal decay, depends crucially on the total momentum resolution.[4] Figure 3.4 shows the branching ratio for internal conversion decays as a function of the energy carried away by the neutrinos. To suppress these backgrounds to an acceptable level, a momentum resolution for the sum of the three electron momenta below 1 MeV is needed.

3.3 Muon Beam and Target

To reach the planned sensitivity a very high number of stopped muons is necessary and therefore a very intense muon beam is required. The MU3E experiment will be run at the Paul Scherrer Institute (PSI) in Switzerland, which operates the world's most powerful proton beam with up to 2.3 mA of 590 MeV/c protons. In two rotating carbon targets, secondary particles are produced. Of interest for the MU3E experiment are the so-

[4] Only electrons with a known and negligible mass are measured. The momentum and energy measurements are equivalent.

Figure 3.5: The shape of the extended target in the longitudinal plane and its position in the muon beam.

called surface muons, which are created from the decays of pions stopped close to the target surface. In a first low intensity phase, the already existing PiE5 beamline can be used. It is currently occupied by the MEG experiment and provides a beam of low momentum surface muons of up to 2×10^8 muons/s. To reach the final sensitivity a muon rate of about 2×10^9 muons/s is required. A new beamline capturing the muons produced in the Swiss Spallation Neutron Source (SINQ) at PSI could provide such a rate and is currently under study [Sch+12].

The incoming muon beam[5] is stopped in an extended hollow double cone target. The arrangement of the target in the beam is illustrated in Figure 3.5. The target is made from thin aluminium with a thickness of $\sim 60\,\mu m$, a length of 10 cm and a radius of 1 cm. Preliminary simulations with this target geometry show that incoming muons with an energy of 28 MeV/c are almost completely stopped and the stopping positions are uniformly distributed over the length and the diameter of the target [Sch+12].

3.4 Electron Tracker

The main detector for the MU3E experiment is a magnetic spectrometer designed to precisely measure the low momentum electrons from the muon decays. It measures the positions of electrons moving in a solenoidal field of ~ 1 T aligned along the beam direction. The total material budget is reduced to minimize the effects of multiple scattering.

3.4.1 Multiple Scattering

Charged Particles traversing a medium will be deflected by electro-magnetic interactions with the nuclei of the material. This effect is called multiple Coulomb scattering due to the underlying Coulomb interaction. The overall effect on the particle trajectory is illustrated in Figure 3.6. On its way

[5]This decay target is different from the carbon production target.

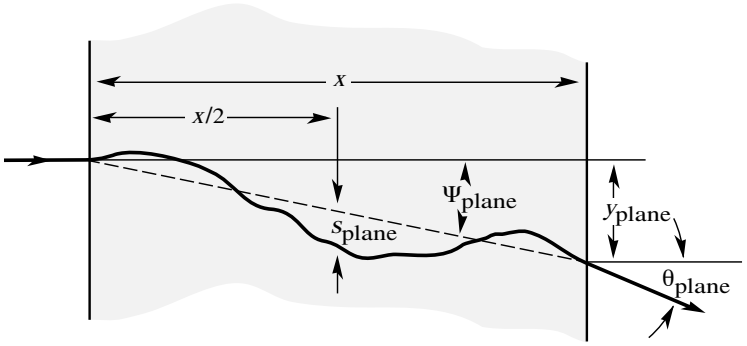

Figure 3.6: The effect of multiple scattering on a particle trajectory. Taken from [Nak+10].

trough the material the particle randomly changes its direction. The overall effect is a displacement and a kink angle with respect to the undisturbed initial trajectory. In the classical description of the scattering the particle momentum is conserved and possible energy losses are neglected. The distribution of the scattering angle projected onto a plane perpendicular to the initial track direction is well described by a Gaussian[6] with a mean of zero and a standard deviation given by the following equation [Nak+10]:

$$\theta_0 = \frac{13.6\,\text{MeV}}{\beta c p} z \sqrt{\frac{x}{X_0}} \left(1 + 0.038 \log\left(\frac{x}{X_0}\right)\right) \tag{3.3}$$

The spread of the angle distribution is inversely proportional to the particle momentum p and scales with a square root of the traversed material thickness x in units of the radiation length X_0. The radiation length is a material constant. z is the charge of the particle. This means that multiple scattering is enhanced for low momentum particles traversing thick materials.

3.4.2 Tracker Design

As described in the previous section, the overall material thickness needs to be reduced as much as possible to minimize the effects of multiple scattering. This entails to use as few detector layers as possible comprised of as little material as possible with a high radiation length.

[6] This is true for small scattering angles up to a few θ_0.

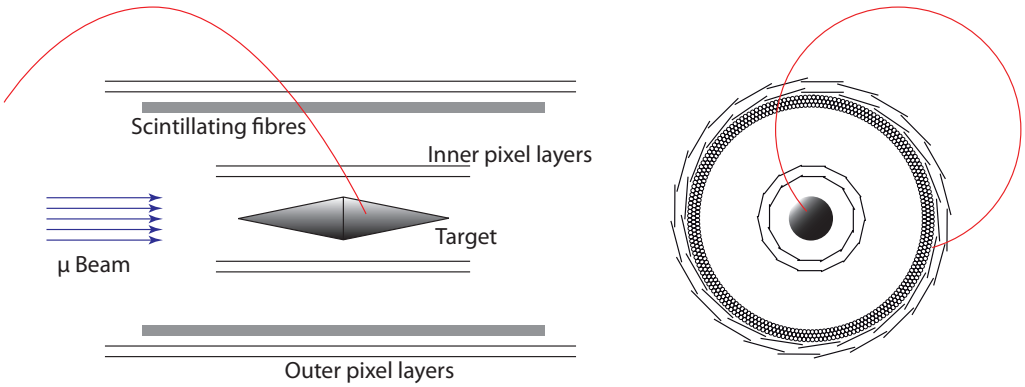

Figure 3.7: A schematic drawing of the MU3E detector baseline design. The red line represents an typical electron track. The length of the detector is not to scale.

The chosen baseline design is shown in Figure 3.7. Four layers of sensors arranged in two double layers are used. This number of measurements allows the reconstruction of a circle with an additional constraint. The inner layers are located close to the target to allow a good vertex resolution. In one doublet, the effects of a scattering angle at the first layer on the position deviation in the second layer are small due to the small track length. This simplifies the track finding procedures.

Each layer is made from high-voltage monolithic active pixel sensors (HV-MAPS) supported by a Kapton® framework. The HV-MAPS allow a fast digital readout, a high geometric coverage and a small pixel size of 80 µm [Per07; PKF10; PT10]. In addition, they can be thinned down to less than 50 µm without compromising their performance. The silicon sensor and the Kapton® support structure add up to a very low combined material budget of less than $0.001 X_0$ [Sch+12].

3.5 Timing Measurements

Additional timing information is required to suppress accidental backgrounds and to allow the identification of coincident signal decay electrons. To this end, scintillating fiber hodoscopes are installed just before the second double layers as shown in Figure 3.7. The total thickness of the hodoscope is of the order of 1 mm to reduce additional multiple scattering effects. They should be read out on both sides with a time resolution of

better than 1 ns [Sch+12].

Chapter 4

Helical Tracks

Track reconstruction methods require a model of the expected particle motion. The physical parameters (charge, momentum and position) that normally describe a particle track are often not optimal in the context of the track reconstruction. Here, the track model for a charged particle in a solenoidal field is derived. An appropriate set of track parameters and their relations to the physical parameters are described. Possible deviations of the particle motion from the idealized track model can be described as uncertainties of the geometrical parameters.

4.1 Equations of Motion

The assumptions of the idealized track model are as follows. A particle of charge q is moving with a speed of $\boldsymbol{v}$ in a solenoidal magnetic field in vacuum. No additional electric field is present. The magnetic field is, without loss of generality, aligned along the z-direction of a global cartesian coordinate system, i.e. $\boldsymbol{B} = B\hat{\boldsymbol{e}}_z$. The charged particle is subject to the following Lorentz-force ([Dem04]).[1]

$$\boldsymbol{F} = qB(\boldsymbol{v} \times \hat{\boldsymbol{e}}_z) \tag{4.1}$$

Hence, the Lorentz-force is perpendicular to the particle trajectory and the corresponding equations of motion $\mathrm{d}\boldsymbol{p}/\,\mathrm{d}t = \boldsymbol{F}$ in the laboratory frame conserve the particle momentum $\boldsymbol{p} = mv\gamma$. They yield the track position $\boldsymbol{x}$ as a function of time. In a tracking environment, only spatial quantities are well measured and the track model should use only those quantities that

[1] Unless stated otherwise, equations are expressed in SI-units.

are directly accessible. Using the conserved momentum $p = \|\boldsymbol{p}\| = m\gamma\beta c$ the equations of motion can be rewritten as functions of the path length s of the track curve[FR00, Chapter 3.3]. With $\mathrm{d}s/\,\mathrm{d}t = v = \beta c$ the following substitutions can be derived.

$$\frac{\mathrm{d}\boldsymbol{x}}{\mathrm{d}t} = \frac{\mathrm{d}\boldsymbol{x}}{\mathrm{d}s}\frac{\mathrm{d}s}{\mathrm{d}t} = \frac{\mathrm{d}\boldsymbol{x}}{\mathrm{d}s}\beta c \tag{4.2}$$

$$\frac{\mathrm{d}^2\boldsymbol{x}}{\mathrm{d}t^2} = \frac{\mathrm{d}}{\mathrm{d}t}\frac{\mathrm{d}\boldsymbol{x}}{\mathrm{d}s}\beta c = \frac{\mathrm{d}^2\boldsymbol{x}}{\mathrm{d}s^2}\beta^2 c^2 \tag{4.3}$$

The equations of motion can then be expressed solely in terms of geometric quantities and form the basis of the idealized track model.

$$\frac{\mathrm{d}^2\boldsymbol{x}}{\mathrm{d}s^2} = \frac{qB}{c}\frac{1}{p}\left(\frac{\mathrm{d}\boldsymbol{x}}{\mathrm{d}s} \times \hat{\boldsymbol{e}}_z\right) \tag{4.4}$$

Equation 4.4 states three second order partial differential equations. In general, six integration constants are needed to fully specify the solutions. Geometrical quantities and the path length can be defined in terms of the infinitesimal path elements of the track curve. This gives rise to the following additional constraint.

$$\mathrm{d}s^2 = \mathrm{d}x^2 + \mathrm{d}y^2 + \mathrm{d}z^2 \iff \left(\frac{\mathrm{d}x}{\mathrm{d}s}\right)^2 + \left(\frac{\mathrm{d}y}{\mathrm{d}s}\right)^2 + \left(\frac{\mathrm{d}z}{\mathrm{d}s}\right)^2 = 1 \tag{4.5}$$

As a result, every solution to the equations of motion can be described by five parameters.

4.2 Track Curve

The solution to the equations of motion in (4.4) is a helix along the z-axis. It can be split up into a circular movement in the (x, y)-plane and a linear movement along the z-direction. The (x, y)-plane is transverse to the magnetic field and is called the transverse plane. The movement along the z-axis is normally described as a function of the path length in the transverse plane. For the sake of simplicity the longitudinal direction will also be called the longitudinal plane of motion (although it is not a geometrical plane).

4.2.1 Position and Tangent

The solution to (4.4) can be written using a set of three unit vectors defined at the initial position at s = 0. They form the basis of a local right-handed

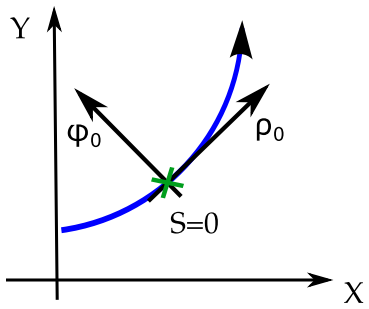

Figure 4.1: The track unit vectors $\hat{\boldsymbol{\varphi}}_0$ and $\hat{\boldsymbol{\rho}}_0$.

coordinate system. To best reflect the two different planes of motion the following unit vectors are chosen.[2]

$$\hat{\boldsymbol{\rho}}_0 = \frac{\hat{\boldsymbol{t}}_0 \times \hat{\boldsymbol{z}}}{\left\|\hat{\boldsymbol{t}}_0 \times \hat{\boldsymbol{z}}\right\|} \tag{4.6}$$

$$\hat{\boldsymbol{\varphi}}_0 = \hat{\boldsymbol{z}} \times \hat{\boldsymbol{\rho}}_0 \tag{4.7}$$

$$\hat{\boldsymbol{z}}_0 = \hat{\boldsymbol{z}} \tag{4.8}$$

The definition of the unit vectors $\hat{\boldsymbol{\rho}}_0$ and $\hat{\boldsymbol{\varphi}}_0$ is illustrated in Figure 4.1.

These unit vectors are defined using the initial track tangent $\hat{\boldsymbol{t}}_0 = \boldsymbol{p}_0/\|\boldsymbol{p}_0\|$ and have the following meaning: $\hat{\boldsymbol{\varphi}}_0$ is the normalized projection of the track tangent into the global (x, y)-plane, $\hat{\boldsymbol{\rho}}_0$ is the unit vector normal to the projected tangent in the global (x, y)-plane and $\hat{\boldsymbol{z}}_0$ is the unit vector of the global z-axis. $\hat{\boldsymbol{\rho}}_0$ and $\hat{\boldsymbol{\varphi}}_0$ span the transverse plane and $\hat{\boldsymbol{z}}$ defines the longitudinal direction. They are also the basis vectors of a cylindrical coordinate system aligned with the z-axis as the cylinder axis. The track position $\boldsymbol{x}$ and the track tangent unit vector $\hat{\boldsymbol{t}} = \partial\hat{\boldsymbol{x}}/\partial s$ at the path length s are defined as follows.[3]

$$\boldsymbol{x} = \boldsymbol{x}_0 - \frac{\alpha}{Q}(1 - \cos\theta)\ \hat{\boldsymbol{\rho}}_0 + \frac{\alpha}{Q}\sin\theta\ \hat{\boldsymbol{\varphi}}_0 + \frac{\gamma}{Q}\theta\ \hat{\boldsymbol{z}} \tag{4.9}$$

$$\hat{\boldsymbol{t}} = -\alpha\sin\theta\ \hat{\boldsymbol{\rho}}_0 + \alpha\cos\theta\ \hat{\boldsymbol{\varphi}}_0 + \gamma\ \hat{\boldsymbol{z}} \tag{4.10}$$

The path length dependency is given by $\theta = Qs$ with $Q = -qB/pc$ being the signed three dimensional curvature of the track curve. The initial

[2] A subscript 0 on a quantity indicates that the value at s = 0 is used.

[3] This is very similar to the definition in [SW06] but with a different set of unit vectors.

position of the track is $\boldsymbol{x}_0$ and the remaining constants are:

$$\alpha = \left\| \hat{\boldsymbol{t}}_0 \times \hat{\boldsymbol{z}} \right\| \tag{4.11}$$

$$\gamma = \hat{\boldsymbol{t}}_0 \cdot \hat{\boldsymbol{z}} \tag{4.12}$$

4.2.2 Decoupling the Circular Movement

It is often useful to decouple the two planes of motion as much as possible. That means that all quantities involved should be defined in only one of the planes. Thus, the curvature and the path length need to be replaced, because they are quantities defined in all three dimensions. The substitution $\kappa = -\alpha Q$ is used to replace the curvature.[4] From equation (4.9) it follows that κ is the curvature of the track projected in the transverse plane, i.e. the curvature of the transverse track circle. The path length is replaced by the projected arc length a of the track circle in the transverse plane using the substitution $a = \sqrt{1-\gamma^2}\, s$. The derivation of this substitution can be found in the appendix in section A.1. Assuming that $s = 0$ and $a = 0$ both correspond to the same initial track position, the track position expression in (4.9) changes as follows.

$$\boldsymbol{x} = \boldsymbol{x}_0 + \frac{1}{\kappa}\left(1 - \cos\theta\right)\ \hat{\boldsymbol{\rho}}_0 - \frac{1}{\kappa}\sin\theta\ \hat{\boldsymbol{\varphi}}_0 + \frac{\gamma}{\alpha}\ a\ \hat{\boldsymbol{z}} \tag{4.13}$$

The expression for the track tangent is identical to the previous one in (4.10). The dependence on the arc length for both the position and the track tangent is now given by $\theta = -\kappa a$.

4.3 Karimaeki Parametrization

The five parameters needed to describe the track can be split up into two sets. Three parameters for the circular motion in the transverse plane and two parameters to describe the linear motion in the longitudinal plane. The circular parameters are the ones defined by Karimäki for the circle fit in [Kar91] as follows.

κ the signed curvature of the track in the (x, y)-plane.

[4] The extra minus sign is an arbitrary choice to bring the definition in line with the curvature definition in [Kar91].

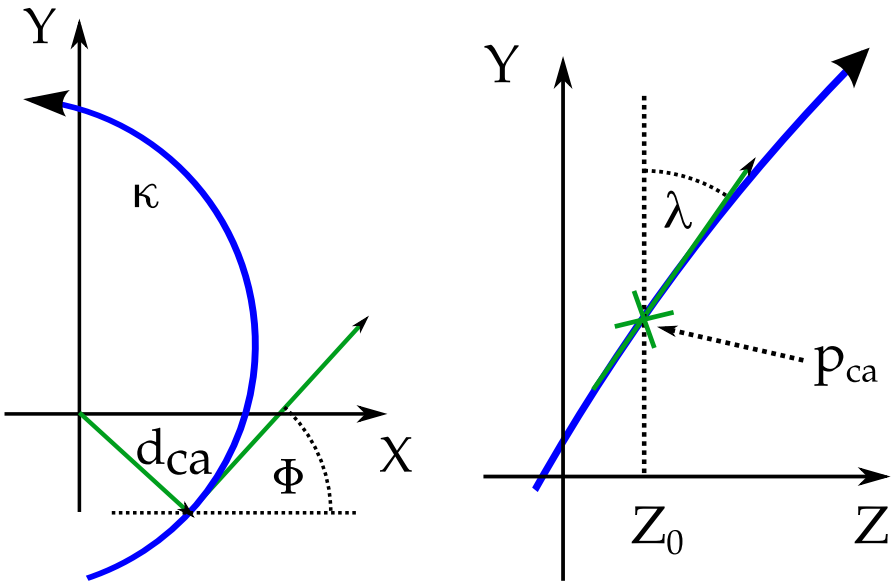

(a) Circular Parameters (b) Linear Parameters

Figure 4.2: The Karimaeki parameters.

ϕ the angle of inclination in the (x, y)-plane at the position of closest approach, i.e. the angle between the x-axis and the projected track tangent.

d_{ca} the signed distance of closest approach in the (x, y)-plane.

These parameter definitions are illustrated in Figure 4.2.

The sign of the curvature κ indicates the direction of movement along the circle. Positive curvature corresponds to a clockwise and a negative curvature to a counter-clockwise rotation. The sign of d_{ca} is indirectly defined by the sign of the product $d_{ca}\kappa$. A negative value of the product indicates that the origin of the transverse coordinate system is located inside the track circle and a positive value indicates that it is located outside of it. An illustration of these sign definitions can be found in Figure 4.3. This sign definition is equivalent to the one in [Kar91] and κ is identical to the transverse curvature defined in the previous section.

The parameters of the linear motion define the intercept and the slope of a straight line in the longitudinal (a, z)-plane.

λ the dip angle between the transverse plane and the longitudinal direction at the initial position, i.e. the angle between the projected track tangent in the (x, y)-plane and the track tangent.

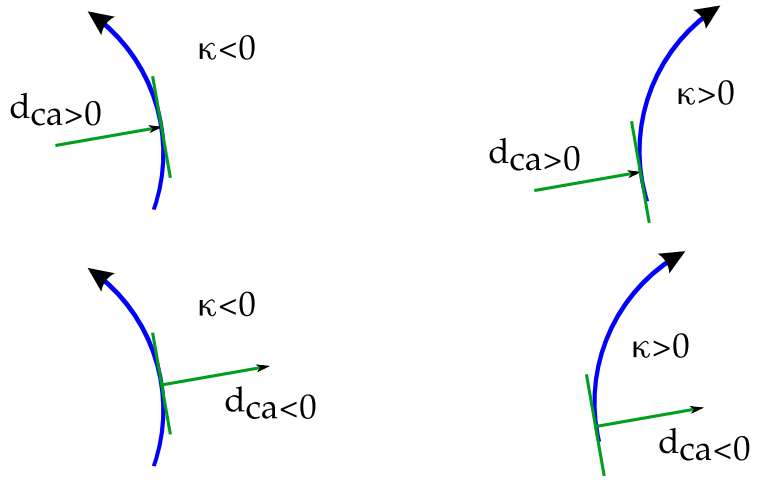

Figure 4.3: The sign definition for d_{ca} and κ.

z_0 the z-position at the initial position.

Using these parameter definitions, the track curve and the tangent are rewritten in a form that depends explicitly on the parameters. First, the initial position $\boldsymbol{x}_0$ is now defined to be the position of closest approach with respect to the origin of the transverse plane. The position of closest approach and the track tangent vector at that position expressed in terms of the Karimaeki parameters are as follows.

$$\boldsymbol{x}_0 = \begin{pmatrix} d_{ca} \sin\phi \\ -d_{ca} \cos\phi \\ z_0 \end{pmatrix} \quad \boldsymbol{t}_0 = \begin{pmatrix} \cos\lambda \cos\phi \\ \cos\lambda \sin\phi \\ \sin\lambda \end{pmatrix} \tag{4.14}$$

Second, the unit vectors defined in section 4.2 and the additional constants α and γ have the following explicit parametrization.

$$\hat{\boldsymbol{\rho}}_0 = \begin{pmatrix} \sin\phi \\ -\cos\phi \\ 0 \end{pmatrix} \quad \hat{\boldsymbol{\varphi}}_0 = \begin{pmatrix} \cos\phi \\ \sin\phi \\ 0 \end{pmatrix} \quad \hat{\boldsymbol{z}} = \begin{pmatrix} 0 \\ 0 \\ 1 \end{pmatrix} \quad \begin{aligned} \alpha &= \cos\lambda \\ \gamma &= \sin\lambda \end{aligned} \tag{4.15}$$

At last, the track position (4.13) is rewritten. The result can be given either in terms of the unit vectors defined above or as a vector in the global

cartesian coordinate system.

$$\boldsymbol{x} = \begin{pmatrix} (d_{ca} + \frac{1}{\kappa}) \sin\phi \\ -\frac{1}{\kappa}\cos\phi \\ z_0 \end{pmatrix} + \begin{pmatrix} \frac{1}{\kappa}\sin(\kappa a - \phi) \\ \frac{1}{\kappa}\cos(\kappa a - \phi) \\ \tan(\lambda)\, a \end{pmatrix} \tag{4.16}$$

Note that the parameter λ only appears as $\tan\lambda$. Consequently, the value of $\tan\lambda$ is used as the track parameter instead of λ.

4.4 Change of Coordinate System

So far, the track parameters are defined with respect to the origin of the global coordinate system, i.e. the origin is the implicit reference point.[5] The initial position of the track at $a = 0$ is the position of closest approach with respect to the origin. Yet, many calculations are greatly simplified if a specific pivot is chosen. For instance, the effects of multiple scattering are best described if the pivot is located at the intersection of the track and the scattering plane. Here, multiple scattering only affects the track angles ϕ and λ while leaving the remaining parameters untouched.

A parameter transformation can be done to select a specific point as the reference point. Figure 4.4 shows the same track and its parameters with two different pivots. The parameter values differ for the two pivots. This illustrates that the track is fully defined only by the combination of its parameters and the chosen reference point.

4.4.1 Parameter Transformation

When moving the track description from a given reference point to another one, a transformation of the corresponding track parameters is needed. The position of closest approach, the track angles and the z_0 position are different in the new system. The transformation can be derived in the following way. Using the track position with the old parameters $\boldsymbol{x}_p$ and $\boldsymbol{\alpha} = (\kappa, \phi, d_{ca}, \tan\lambda, z_0)^T$, the track position and the corresponding arc length a for which the track position is closest to the new pivot $\boldsymbol{x}'_p$ in the transverse plane is derived. For this new position of closest approach the tangent vector and the two remaining unit vectors are obtained similar to the original derivation of the Karimaeki parameters in section 4.3. The

[5] The terms reference point, pivotal point or pivot are used interchangeably.

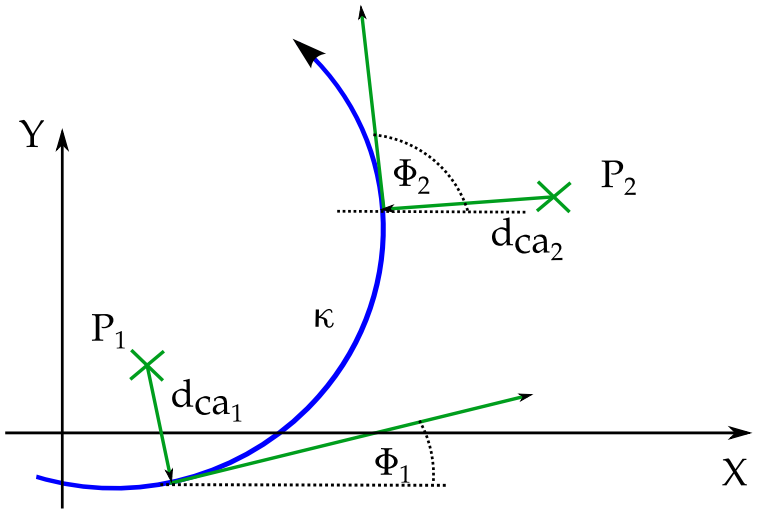

Figure 4.4: The same track and its transverse parameters for two different pivotal points p_1 and p_2.

new parameters $\boldsymbol{\alpha}' = (\kappa', \phi', d'_{ca}, \tan\lambda', z'_0)^T$ can be derived with respect to these unit vectors.

The resulting transformation equations for the transverse parameters can be found in [Kar91] and in [Gro97] for the longitudinal parameters.

$$\begin{aligned} \kappa' &= \kappa \\ \phi' &= \text{atan2}(B, C) \\ d'_{ca} &= (1+U)^{-1} A \\ \tan\lambda' &= \tan\lambda \\ z'_0 &= (z_p - z'_p) + z_0 - \tfrac{\tan\lambda}{\kappa}(\phi' - \phi) \end{aligned} \tag{4.17}$$

These transformations describe the new parameters (primed) as functions of the old parameters (unprimed) and the old and new pivotal points $\boldsymbol{x}_p$ and $\boldsymbol{x}'_p$. The two parameter function $\text{atan2}(y, x)$ is mostly identical to the regular inverse tangent with the quotient of y and x as an argument $\arctan(y/x)$. In addition, it also takes into account the quadrant the coordinates lie in and returns the azimuth angle in the full range $-\pi$ to π or 0 to 2π. The additional constants A, B, C and U depend on the aforementioned

quantities and are given below.

$$u = 1 + d_{ca}\kappa \tag{4.18}$$

$$A = 2\Delta_\perp + \kappa\left(\Delta_\perp^2 + \Delta_\parallel^2\right) \tag{4.19}$$

$$B = \kappa(x_p - x'_p) + u\sin\phi \tag{4.20}$$

$$C = -\kappa(y_p - y'_p) + u\cos\phi \tag{4.21}$$

$$\Delta_\perp = (x_p - x'_p)\sin\phi - (y_p - y'_p)\cos\phi + d_{ca} \tag{4.22}$$

$$\Delta_\parallel = (x_p - x'_p)\cos\phi + (y_p - y'_p)\sin\phi \tag{4.23}$$

$$U = \sqrt{1 + \kappa A} \tag{4.24}$$

Since the track position in the transverse plane is periodic, ϕ and ϕ' are defined only up until additional terms of multiples of 2π. Hence, the transformation of z_0 has multiple branches that differ by multiples of $2\pi\tan\lambda/\kappa$.

4.4.2 Covariance Matrix Transformation

The track parameters may have an associated covariance matrix which needs to be propagated to the new reference point. In the context of error propagation, the old and new reference points are only arbitrary constants because they do not have an associated error. The new parameters $\boldsymbol{\alpha}' = (\kappa', \phi', d'_{ca}, \tan\lambda', z'_0)^T$ can therefore be viewed as functions of the old parameters only, i.e. $\boldsymbol{\alpha}' = \boldsymbol{\alpha}'(\boldsymbol{\alpha})$ and the covariance matrix Σ' of the transformed parameters can be calculated from the covariance matrix Σ of the original parameters and the Jacobian matrix $J = (\partial\alpha'_i/\partial\alpha_i)$ of the parameter transformation using the following matrix equation:

$$\Sigma' = J\Sigma J^T \tag{4.25}$$

The expressions for each element can be found in section A.1 in the appendix.

4.5 Momentum

In the general description of the track curve in section 4.2, the relation between the track curvature and the track momentum is straightforward: $Q = -qB/cp$ (where Q is the track curvature in three dimensions). This

is not the case in the Karimaeki parametrization, because the curvature parameters κ describes the curvature only in the transverse plane. As a result, it only contains information about the transverse momentum, i.e. the length of the momentum vector projected onto the transverse plane. It can be calculated using the following expression [FR00]:

$$p_T = \frac{qB}{c}\frac{1}{\kappa} \tag{4.26}$$

To compute the full momentum, additional parameters are needed. The full momentum vector is defined by $\boldsymbol{p} = p\hat{\boldsymbol{t}}$. From this expression and the definition of the tangent vector in terms of the Karimaeki parameters it follows that the full momentum is given by:

$$p = \cos(\lambda)\ p_T = \frac{qB}{c}\ \frac{\cos\lambda}{\kappa} \tag{4.27}$$

In the Karimaeki parametrization, $\tan\lambda$ is used as the track parameter and $\cos\lambda$ should be expressed in terms of $\tan\lambda$ instead.

$$p = \frac{qB}{c}\ \frac{1}{\sqrt{1+\tan^2\lambda}}\ \frac{1}{\kappa} \tag{4.28}$$

Chapter 5

Track Fitting

In the previous chapter 4, the track model and its geometrical parameters where derived. Using the track model, the particle position and the geometrical track parameters can be calculated at each point along the track curve. For track fitting the sequence is reversed. Starting from a set of measured particle positions the (geometrical) track parameters that best describe the measurements should be estimated.

Track fitting algorithms can differ in their treatment of uncertainties and their correlations as well as computational complexity, e.g. iterative vs. direct algorithms. In the following chapter two non-iterative procedures, a fast helix fit based on Karimaeki's [Kar91] fast circle fit and the broken lines fit by Volker Blobel [Blo06] are introduced and the mathematical details of their implementations are explained.

For this to work, I assume that the connected problem of track finding has already been solved, i.e. the correct subset of detectors hits that belong to a single track has already been selected.

5.1 Tracking Regimes

Depending on the dominating type of uncertainties, two different regimes can be identified: the spatial regime and the scattering regime. The first one is dominated by the spatial uncertainties of the measurements, i.e. by the resolution of the detector itself, whereas the second one is dominated by the uncertainties induced from multiple scattering. Other possible sources of uncertainty, e.g. the energy loss of a particle while traversing the detector, are neglected in this discussion. This is well motivated by the very low total radiation length ($\sim 10^{-3}\ X_0$) of the MU3E detector.

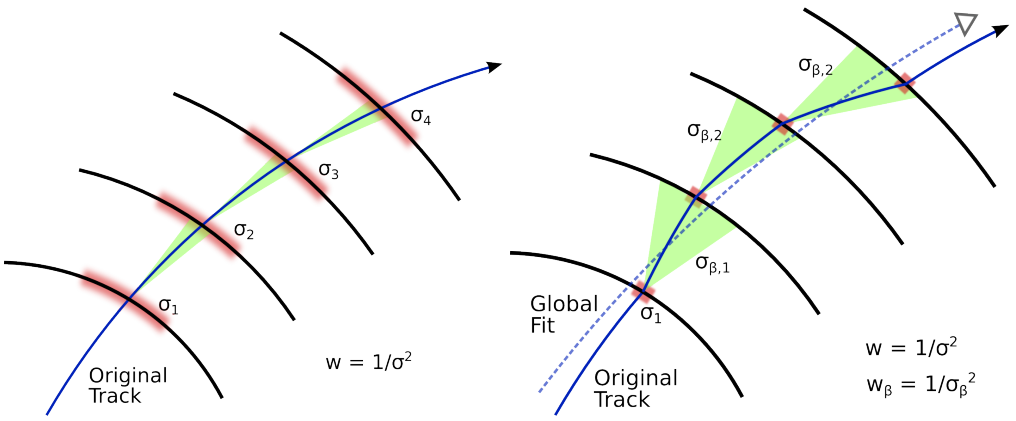

(a) Spatial Regime (b) Scattering Regime

Figure 5.1: Particle trajectories in different tracking regimes. In (a) the uncertainty from spatial measurements is dominating and in (b) the dominating uncertainty comes from multiple scattering. Spatial uncertainties are marked with red bands and scattering angles variances are indicated as green bands.

To illustrate the two different regimes, Figure 5.1 shows the propagation of an example track and the associated errors for both regimes. The detector resolution is marked with red bands and the uncertainties from multiple scattering as green bands.

For dominating spatial errors (5.1a), the resulting measurements are independent. The position measurements at the last layers is not affected by the interactions with the initial ones. This is usually the case for particles with very large momenta, e.g at the Large Hadron Collider, or for detectors with a low spatial resolution.

For the scattering regime, shown in 5.1b, the measurements are heavily correlated. A high angle scattering event at one of the first layers introduces additional deviations for all the following measurements. If the track parameters at the beginning of the tracks are to be determined these parameters are greatly influenced by the measurements at the last layers. Low momenta and high spatial resolutions favor this regime, as it is the case for the MU3E experiment.

5.2 The Method of Least Squares

Before introducing the track fitting procedures it is necessary to define a measure of what the *best-fit* parameters are, i.e. what the output of the track fit should be. To achieve this, the measured positions are assumed to be the result of a particle moving according to a track model with additional statistical noise from the measurement uncertainties. Estimating the optimal parameters of a statistical model can be done using the principle of maximum likelihood [Cow04], i.e. the best-fit parameters are the ones that maximize the likelihood function of the model given the measurements.

In the special case of independent and normally distributed errors maximizing the likelihood is equivalent to minimizing the corresponding sum of squared residuals of the model and the measured data [Cow04]. The residuals are the differences between measurements y_i and corresponding model predictions $f_i = f_i(\boldsymbol{\alpha})$ where the model predictions are functions of the model parameters α_i. Each residual is weighted according to the measurements. The weights are defined as the inverse of the variance of each measurement $w_i = 1/\sigma_i^2$. For a set of N measurements the sum of squared residuals is then defined as follows.

$$S = \sum_{i=1}^{N} w_i r_i^2 = \sum_{i=1}^{N} \frac{(y_i - f(\boldsymbol{\alpha})_i)^2}{\sigma_i^2} \tag{5.1}$$

The best-fit parameters, those that maximize the original likelihood function, are the solutions to the following normal equations:

$$\frac{\partial S}{\partial \alpha_k} = 2 \sum_{i=1}^{N} w_i r_i \frac{\partial r_i}{\partial \alpha_k} = -2 \sum_{i=1}^{N} w_i r_i \frac{\partial f_i}{\partial \alpha_k} = 0 \tag{5.2}$$

Solving this equation for general, i.e. non-linear, models requires an iterative approach. This is computationally expensive and may suffer from numerical instabilities and convergence problems. A direct, non-iterative solution can be found if only linear models are considered. In that case, the residuals can always be written in the following form, where $F = (F_{ij})$ is the coefficient matrix of the model that connects the parameters and the predictions.

$$r_i = y_i - \sum_{j=1}^{M} F_{ij} \alpha_j \implies \frac{\partial r_i}{\partial \alpha_k} = -F_{ik} \tag{5.3}$$

As a result, the solution to the normal equations can be found by solving the following system of linear equations.[1]

$$F^T W F \boldsymbol{\alpha} - F^T W \boldsymbol{y} = 0 \iff \boldsymbol{\alpha} = (F^T W F)^{-1} F^T W \boldsymbol{y} \tag{5.4}$$

W is the diagonal weight matrix with $W_{ii} = w_i$, which is computed from the diagonal measurement covariance matrix $W = \Sigma^{-1}$ as defined above. Minimizing the sum of least squares is now reduced to solving a set of linear equations. This is a problem that can be done quite easily on a computer and many algorithms are readily available to either invert the matrix $F^T W F$ or solve the equation using matrix factorization (e.g. [LAP]). The matrix inversion of $F^T W F$ (a NxN matrix) has a complexity $\mathcal{O}(N^3)$, cubic in the number of measurements. If the matrix is not a full matrix but a sparse matrix, e.g. banddiagonal, faster solutions are available. Solving an NxN banddiagonal matrix scales linearly with the number of entries.

In addition to the best-fit parameters, the least-squares method provides estimates of the parameter errors. At the minimum of the sum of squared residuals (5.1), the parameters are linear functions of the measurements. This is obvious for the linear case, as can be seen in (5.4). For the general case the model function can be linearized around the optimal parameters and a similar expression can be constructed using the Jacobian instead of the coefficient matrix F. The covariance matrix of the best-fit parameters can then be calculated using simple propagation of uncertainty. Due to the relation of the weight matrix and the measurement covariance this reduces to the following expression in the linear case.[2]

$$\Sigma_\alpha = \left(F^T W F\right)^{-1} \tag{5.5}$$

5.2.1 Limitations and Generalizations

Using the linear least square method transforms a complex optimization problem to a linear algebra problem with a significantly reduced computational complexity. That also means that a linear track model is required to take full advantage of this transformation. This is not the case for the helical track model derived in chapter 4. However, as will be shown in the next section, a clever choice of parameters allows a sufficiently precise linear approximation over a wide area of the sensible parameter space.

[1] A full derivation can be found in the appendix Equation A.14

[2] The full derivation can be found in the appendix Equation A.17

In the derivation of the least square method, independent and uncorrelated measurements were assumed. This is not necessarily true, e.g. for multiple scattering, but it works as a first approximation. To fully accommodate also for correlated measurements, the least-squares method can be generalized to non-diagonal measurement covariance matrices. In that case, the weight matrix $W = \Sigma^{-1}$ and consequently also the matrix representing the normal equations $F^T W F$ are dense matrices instead of sparse, diagonal matrices. No optimized algorithms for the solution (inversion) can be used and the complexity is always $\mathcal{O}(N^3)$. That means that by using ordinary linear least square minimization one trades computational complexity at the expense of a correct description of errors and correlations.

5.3 Fast Helix Fit

The fast helix fit (FH) is a global, non-iterative fit of the full track helix. It is based on a factorization of the full 3d fit into two 2d fits, namely a circle fit in the transverse plane and and a straight line fit in the projected longitudinal plane. It assumes uncorrelated measurements and allows a very fast fit for a given set of measurements.

5.3.1 Overview

The fast helix fit uses the Karimaeki parametrization of the track model defined in section 4.3 without consideration of multiple scattering by construction. The selected parameters split up naturally into two groups: three parameters (κ, ϕ, d_{ca}) to describe the circle and two parameters ($\tan\lambda$, z_0) to describe the straight line along the z-direction. Both parameter groups are fitted separately. Possible correlations between them will therefore be neglected. In general, this results in a degraded resolution. The full fit is done in the following order:

1. A circle is fitted to the projected measurements in the (x, y)-plane.
2. The arc length a in the transverse plane is calculated from the fitted circle parameters and the measurements.
3. A straight line is fitted to the measurements in the longitudinal (a, z)-plane.
4. The resulting fitted parameters and their covariance matrix are combined.

5.3.2 Karimaeki's Fast Circle Fit

The circle fit developed by Karimaeki [Kar91] is based on the least squares method described in section 4.3 above. It uses the Karimaeki parametrization of the track model and employs additional approximations to allow a direct calculation of the best-fit parameters. According to the track model, all track positions in the transverse (x, y)-plane should lie on a single circle. This allows the residual expression to be defined in terms of differences in radii, instead of differences in two-dimensional positions as function of the arc length.

For a circle defined by its center and its radius, the residuals are calculated as the difference between the model radius and the measured radius in the coordinate system where the circle center is the origin: $r_i = R_{i,\text{measured}} - R$. Bringing the R term onto the left side, squaring both sides and multiplying them out, one arrives at the following expression:

$$r_i = \frac{(x_i - c_x)^2 + (y_i - c_y)^2 - R^2}{-2R} + \frac{r_i^2}{2R} \tag{5.6}$$

Here, c_x and c_y are the circle center positions in the global cartesian coordinate system. The last term can be dropped if we assume that $|r_i| \ll R$. For the MU3E experiment the residuals are of the order of a few mm (pixel size plus multiple scattering) and the circle radii are in the range of 3 cm to 17 cm. Hence, the former assumption to neglect the second term is well motivated.

The final residual expression is constructed by replacing the naive parameters c_x, c_y and R with the Karimaeki circle parameters κ, ϕ and d_{ca} defined in section 4.3.

$$r_i = \tfrac{1}{2}\kappa(x_i^2 + y_i^2 + d_{ca}^2) - (1 + d_{ca}\kappa)(x_i \sin\phi + y_i \cos\phi) + d_{ca} \tag{5.7}$$

Using this expression for the residuals, the sum of squares written in a slightly different form:

$$S = (1 + d_{ca}\kappa)^2 S' = (1 + d_{ca}\kappa) \sum_{i=0}^{N} w_i r_i' \tag{5.8}$$

r_i' is the remainder of the residual expression after factoring out the $(1 + d_{ca}\kappa)$ term. Instead of minimizing the original sum S, the reduced sum S' is minimized. According to [Kar91], this only introduces a negligible additional error on the resulting parameters for hit positions close to

the origin, i.e. d_{ca} is small with respect to κ. This approximation enables the calculation of an explicit solution to the normal equations that only requires a fixed set of sums over the single measurements x_i and y_i and their combinations. The calculation of the parameter covariance matrix requires only little additional time because all the information is already contained in the sums calculated for the fit. The full procedure, the non-iterative solution for the fitted parameters and the covariance matrix can be found in [Kar91].

Using the fitted parameters, the arc length a_i for each measurement can be calculated. First, the measured coordinates are transformed into a system were the origin coincides with the center of the track circle.

$$\begin{pmatrix} x_i' \\ y_i' \end{pmatrix} = \begin{pmatrix} \sin\phi_0 & -\cos\phi_0 \\ \cos\phi_0 & \sin\phi_0 \end{pmatrix} \begin{pmatrix} x_i \\ y_i \end{pmatrix} - \begin{pmatrix} d_{ca} + \frac{1}{\kappa} \\ 0 \end{pmatrix} \tag{5.9}$$

In this system we can calculate the track angle θ_i, i.e. the azimuth angle of (x_i', y_i'). We have to take into account that tracks with positive curvature start at $(-r, 0)$ and tracks with negative curvature at $(r, 0)$ with $r = \left|1/\kappa\right|$.

$$a_i = r \begin{cases} \operatorname{atan2}(y_i',\, x_i') & \kappa \leq 0 \\ \operatorname{atan2}(y_i',\, -x_i') & \kappa > 0 \end{cases} \tag{5.10}$$

5.3.3 Straight Line Fit

As shown in section 4.2, the position along the z-axis is a linear function of arc length in the transverse plane. Using the fitted arc length from the circle fit and the measurements the residual expression can be defined as follows.

$$r_i = z_i - z_0 - \tan\lambda\, a_i \tag{5.11}$$

This is only linearly dependent on the parameters z_0 and $\tan\lambda$. The method of linear least squares can be applied directly as described above. An explicit solution to the normal equation exists with only a linear complexity with respect to the number of measurements (see e.g. [Pre92, chapter 15.]).

5.3.4 Weights

For the first fit the initial weights are calculated from the known variances of the spatial measurements as $w_i = 1/\sigma_i^2$.

5.4 Broken Lines Fit

The broken lines (BL) fit [Blo06] is a detailed refit of the residuals from a previous helix track fit ("seed") that takes into account the effects of multiple scattering. In its original form, the BL is a two dimensional fit. For the full refit of the three dimensional helix, it has to be used twice in two different planes. The fit procedure is explained for tracks with or without curvature.

5.4.1 Straight Tracks

For the simple case we assume tracks that propagate without curvature. This would be the case, e.g. for the motion of very high momentum particles in the transverse plane or for the drift motion of a particle along the magnetic field axis.

Residuals ϵ_i are calculated from the measurements y_i and the track seed. The track seed also provides the travelled distance l_i for every residual axis. The points (l_i, ϵ_i) are the transformed measurements in the local system of the track. For all further calculations it is assumed that movement along the residual axes is independent of the position on the track, i.e. that the residual axes are perpendicular to the track.

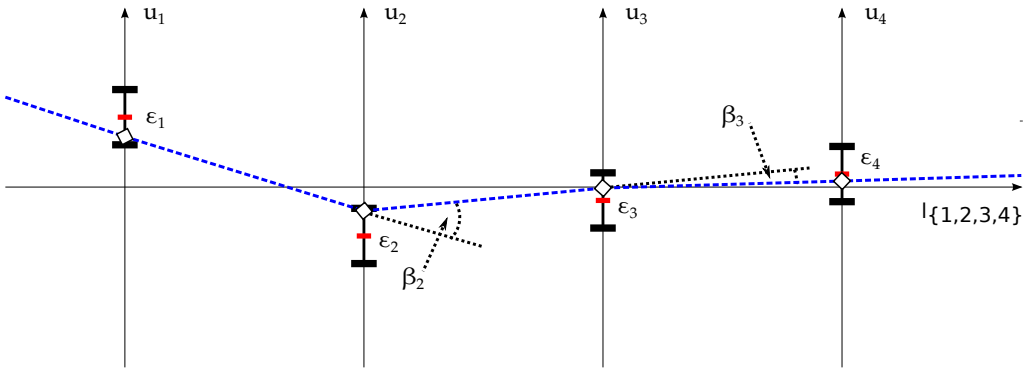

Figure 5.2: The residual system of the track. It shows the initial residuals (red dash) with their errors (thick black dashes), the new intersection points (hollow diamonds) and the resulting track trajectory (blue dashed line) as a function of the travelled track length.

A new trajectory is defined by a set of intersection points u_i between the track and each residual axis. Figure 5.2 shows an example configuration

of the new trajectory in the residual system. The new trajectory (marked with a dashed blue line) is not a single straight track. Instead, we have kink angles β_i at every residual axis. Their values can be calculated from neighboring intersection points except for the first and the last one. Assuming that these kink angles are small the following linearized expression can be used.

$$\beta_i = \delta_{i-1} u_{i-1} - (\delta_{i-1} + \delta_i) u_i + \delta_i u_{i+1} \quad \text{with } \delta_i = (l_{i+1} - l_i)^{-1} \tag{5.12}$$

The BL fit calculates the new trajectory by finding the set of intersection points that minimizes both the distance to the initial residuals and the kink angles at every residual axis. The objective function for the corresponding least squares problem can be broken up into to parts. The first one relates to the detector resolution and the second one to the kink angles. Both parts are weighted linear least squares problems.

$$S = S_\epsilon + S_\beta = \sum_{i=1}^{N} w_i (\epsilon_i - u_i)^2 + \sum_{i=2}^{N-1} w_{\beta,i} \beta_i^2 \tag{5.13}$$

The weights w_i are calculated from the known detector resolution projected to the plane transverse track, i.e. $w_i = \sigma_i^{-2}$. The weights $w_{\beta,i} = \sigma_{\beta,i}^{-2}$ for the kink angles can be calculated using the equation (3.3) from multiple scattering theory [Nak+10, Chapter 27.3.]. Assuming that we have this scatterer at each measurement axis, the expected scattering angle variance $\sigma_{\beta,i}^2$ can be calculated from the effective detector thickness and the particle momentum. The detector thickness should be known a priori and the approximate particle momentum can be calculated from the initial track seed.

$$\frac{\partial S_\epsilon}{\partial u_i} + \frac{\partial S_\beta}{\partial u_i} = 0 \tag{5.14}$$

The solution to the normal equations (5.14) can be split up and each part can be solved according to section 5.2 for the same set of parameters $\boldsymbol{u} = (u_1, u_2, \cdots, u_N)^T$. For the first part S_ϵ this yields the following normal equations:

$$\left(\frac{\partial S_\epsilon}{\partial u_i} \right) = W\boldsymbol{u} - W\boldsymbol{\epsilon} = 0 \tag{5.15}$$

The normal equations for the second part S_ϵ are:

$$\left(\frac{\partial S_\beta}{\partial u_i} \right) = (F_\beta^T W_\beta F_\beta)\boldsymbol{u} = 0 \tag{5.16}$$

With the following definition for the matrix F_β:

$$F_\beta = \begin{pmatrix} 0 & 0 & & & \\ B_{21} & B_{22} & B_{23} & & \\ & B_{32} & B_{33} & B_{34} & \\ & & \ddots & \ddots & \ddots \\ & & & 0 & 0 \end{pmatrix} \qquad \begin{aligned} B_{ii-1} &= \delta_{i-1} \\ B_{ii} &= \delta_{i-1} + \delta_i \\ B_{ii+1} &= \delta_i \end{aligned} \tag{5.17}$$

The combined normal equations from the two parts can be written in the form $C_u \boldsymbol{u} - \boldsymbol{r}_u = 0$ where $\boldsymbol{r}_u = W\boldsymbol{\epsilon}$ is an N-dimensional vector and $C_u = W + F_\beta^T W_\beta F_\beta$ is a symmetric band diagonal NxN matrix.

$$C_u = \begin{pmatrix} C_{11} & C_{12} & C_{13} & & & & \\ C_{21} & C_{22} & C_{23} & C_{24} & & & \\ C_{31} & C_{32} & C_{33} & C_{34} & C_{35} & & \\ & C_{42} & C_{43} & C_{44} & C_{45} & C_{55} & \\ & & \ddots & \ddots & \ddots & \ddots & \ddots \end{pmatrix} \tag{5.18}$$

$$C_{u,ij} = \delta_{ij} w_i + \sum_{k=2}^{N-1} w_{\beta,k} F_{ki} F_{kj}$$

The band diagonal form allows for a fast solution in linear time using the Cholesky decomposition of C_u [Blo06].

The parameter covariance matrix can be calculated as defined in section 5.2, however special care is required in the calculations. The expected kink angles are zero and have an associated covariance matrix, the expected variance from multiple scattering theory. They have to be treated as virtual measurements and enter the covariance calculations. If we assume that the residuals ϵ_i and the 'measured' kink angles are independent and are weighted according to their measurement variance, i.e. $\Sigma_\epsilon = W^{-1}$ and $\Sigma_{\beta_0} = W_\beta^{-1}$, the covariance matrix for $\boldsymbol{u}$ simplifies to:

$$\Sigma_u = (W + F_\beta^T W_\beta F_\beta)^{-1} = C_u^{-1} \tag{5.19}$$

5.4.2 Curved Tracks

For a curved track, the fitting procedure needs to be modified. The residuals are now calculated in the curvilinear system of the initial track fit and should again be defined along axes perpendicular to the track. Figure 5.3

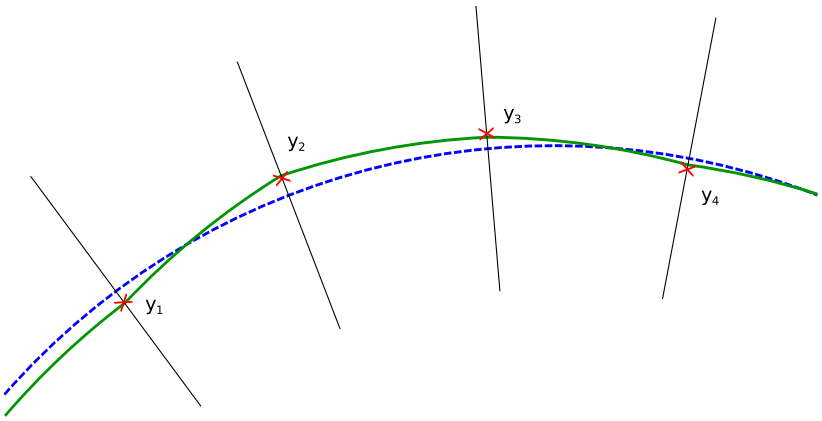

Figure 5.3: A particle trajectory in the presence of multiple scattering (solid green line), the registered hit positions (red crosses) and the initial global circle fit (dashed blue line)

shows an example configuration of a curved particle trajectory influenced by multiple scattering and the initial circle fit. It can be seen that the additional scattering angles have a strong impact on the fitted track curvature.

In the straight track case it is assumed that the geometrical kink angles in the residual system in Figure 5.2 originate only from multiple scattering. This is not true for the curved track case. A curvature difference between

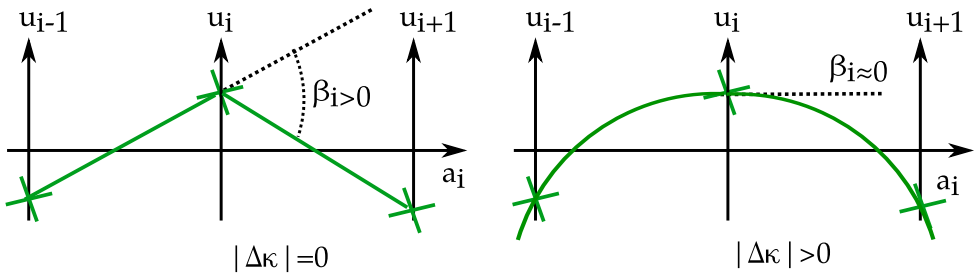

Figure 5.4: Two different trajectories that result in the same positions in the residual system. On the left side, the seed correctly estimates the curvature and the residuals originate only from multiple scattering. On the right side, no multiple scattering occurred and the residuals are only due to a mismeasured initial curvature.

the true track and the initial seed would also result in a kink angle in the curvilinear system. Figure 5.4 shows two possible trajectory configurations

for a given set of residuals. In the left configuration, the initial estimate of the track curvature is already correct and the geometric kink angles originate only from multiple scattering. For the right configuration, the actual scattering angle vanishes and the measured geometric kink angle arises only from a mismeasured curvature. The definition of the scattering angles used in the curved broken lines fit needs to take these two possibilities into account. This is done by adding a global curvature correction $\Delta\kappa$ to the definition of the fitted scattering angles that modifies the geometric kink angles calculated from the intersection points u_i.

$$\beta_i = \delta_{i-1}u_{i-1} - (\delta_{i-1} + \delta_i)u_i + \delta_i u_{i+1} + \tfrac{1}{2}(a_{i-1} + a_i)\Delta\kappa \tag{5.20}$$

$$a_i = \sqrt{(l_{i+1} - l_i)^2 + (\epsilon_{i+1} - \epsilon_i)^2} \tag{5.21}$$

There are are now N+1 parameters $\boldsymbol{u} = (\Delta\kappa, u_1, u_2, \cdots)^T$. The general expression for the objective function in (5.13) does not change but the resulting normal equations are modified slightly due to the different defintion of β_i.

$$\frac{\partial S}{\partial u_i} = \begin{cases} \frac{\partial S_\beta}{\partial \Delta\kappa} & i = 0 \\ \frac{\partial S_\beta}{\partial u_{i-1}} + \frac{\partial S_\epsilon}{\partial u_{i-1}} & i \geq 1 \end{cases} = 0 \tag{5.22}$$

No changes are introduced to the normal equations derived from S_ϵ except for additional zeros to correct the shape. For the normal equations derived from S_β the matrix F_β is modified and has a NxN+1 shape.

$$F_\beta = \begin{pmatrix} 0 & 0 & 0 & & & \\ A_2 & B_{21} & B_{22} & B_{23} & & \\ A_3 & & B_{32} & B_{33} & B_{34} & \\ \vdots & & & \ddots & \ddots & \ddots \\ 0 & & & & 0 & 0 \end{pmatrix} \tag{5.23}$$

B_{ij} are the known values from the straight track case and A_i is defined as:

$$A_i = \tfrac{1}{2}(a_{i-1} + a_i) \tag{5.24}$$

The combined normal equations can be written in the form $C\boldsymbol{u} - \boldsymbol{r} = 0$ where $\boldsymbol{u}$ and $\boldsymbol{r}$ are N+1-dimensional vectors and $C = W + F_\beta^T W_\beta F_\beta$ [3] is a

[3] W needs to be padded with one column and one row of zeros to correct its shape towards a N+1xN+1 matrix.

symmetric N+1xN+1 matrix with the following contents :

$$\begin{pmatrix} K & \boldsymbol{k}^T \\ \boldsymbol{k} & C_u \end{pmatrix} \begin{pmatrix} \Delta\kappa \\ \boldsymbol{u} \end{pmatrix} - \begin{pmatrix} 0 \\ \boldsymbol{r}_u \end{pmatrix} = 0 \tag{5.25}$$

C_u and $\boldsymbol{r}_u$ are defined in the same way as in the straight track case. The additional scalar K and N-dimensional vector $\boldsymbol{k}$ is defined as:

$$K = \sum_{k=2}^{N-1} w_{\beta,k} A_k^2 = \tfrac{1}{4} \sum_{k=2}^{N-1} w_{\beta,k} (a_{k-1} + a_k)^2 \tag{5.26}$$

$$k_i = \sum_{k=2}^{N-1} w_{\beta,k} A_k B_{ki} = \tfrac{1}{2} \sum_{k=2}^{N-1} w_{\beta,k} (a_{k-1} + a_k) B_{ki} \tag{5.27}$$

Even though the matrix C does not have a pure band diagonal shape anymore, a fast solution in linear time is still possible and can be found in [Blo06]. The calculation of the covariance matrix is identical to the calculation in the straight track case and again yields $\Sigma_{\Delta\kappa,u} = C^{-1}$.

5.4.3 Parameter Corrections

The fit parameters of the broken lines fit are the new trajectory position u_i in the residual system. From these, corrections to the initial track parameters can be calculated. Since all the parameters are locally defined, the parameter corrections are given with respect to one of the intersections. To accurately determine the initial track parameters, the intersection between the track and the first layer is chosen. This reduces the effects of correlations at later measurements as far as possible.

In the transverse plane, the curved broken lines fit is used. The correction to the curvature is a global parameter and a direct result of the refit. The distance of closest approach to the chosen intersection is just the estimated track intersection u_1, since the reference point is located on the track curve itself. The correction to the initial track angle ϕ is derived from the slope of the trajectory between the first two positions in the residual system. The corresponding mathematical expression are:

$$\begin{aligned} \Delta d_{ca} &= d_{ca} = u_1 \\ \Delta\phi &= \frac{u_2 - u_1}{l_2 - l_1} \end{aligned} \tag{5.28}$$

The covariance matrix of the corrected parameters can be calculated using propagation of uncertainties using the covariance matrix Σ_u of the fitted trajectory positions. However, the derived correction neglects a possible

scattering angle at the first layer. To account for this additional uncertainty the variance of the scattering angle distribution is added to the ϕ variance.

$$\sigma_{\phi}^2 = \sigma_{u}^2 + \sigma_{\beta,1}^2 \tag{5.29}$$

In the above equation, σ_{u}^2 is the result of the propagation of uncertainties from (5.28) and $\sigma_{\beta,1}^2$ is calculated according to (3.3) using the parameters from the initial fit.

Chapter 6

Implementation and Results

To test and compare the performance of the track fitting algorithms described in the previous chapter, I implemented both algorithms and a simulation using Python [Fou; J+–]. In this chapter, the details of the implementation and the resulting performance for different detector geometries are explained.

6.1 Simulation

Since we are not interested in a detailed study of the detector geometry, but in a comparison of the different tracking algorithms, a full detector simulation, e.g. using GEANT4 [Ago+03], is not required. Instead, a specialized simulation is implemented based on the track parametrization defined in chapter 4 and a simplified detector geometry. This allows full control over each step of the simulation and is a specific setup tailored to test the fit algorithms itself. It also gives access to all the true information generated at every stage of the process.

6.1.1 Generators

For my studies I only used events containing a single track each, with different parameter distributions for the initial state. The simulated tracks are not generated in terms of the physical parameters such as initial position and momentum, but already at the level of the geometric parameters defined in section 4.3. The reference point is set to be the origin of the coordinate system.

For the initial studies the following track generator is employed. All generated tracks have the same set of initial parameters and the only differences come from the simulation of uncertainties. For the final studies the tracks parameters are drawn from uniform distributions. The limits for each parameter are setup to mimic the distributions that are expected from the target shape, i.e. $\kappa = \pm 5.0\,\mathrm{m}^{-1}$ to $\pm 20\,\mathrm{m}^{-1}$, $\phi = 0$ to 2π and $d_{ca} = -1.0\,\mathrm{cm}$ to $1.0\,\mathrm{cm}$.

6.1.2 Geometry

Instead of the geometry defined in chapter 3, a simplified geometry is used during the simulation. The real detector is build from a set of planar sensors that form a polygonal shape in the transverse plane as shown in Figure 3.7. However, the number of sensors is high enough that a purely cylindrical shape is a sufficient approximation. Hence, each detector layer is simulated as a cylinder with a fixed radius centered around the z axis to simplify the simulation. The length of the cylinder is not restricted and the geometrical acceptance (in terms of the dip angle) is reproduced by the limits of the initial track parameters.

6.1.3 Track Propagation and Multiple Scattering

The generated particle is assumed to behave according to the ideal track model defined in chapter 4. This, in combination with the cylindrical detector shape, allows a propagation of the track using an explicit analytical expression for the hit position. Starting from the initial position, the hit position at each detector layer is calculated using the intersection of the helical track with the cylindrical surface. After the calculation of the hit position, the pivot of the track description is moved to the hit position.

Multiple scattering at the detector layer is then simulated by altering the track parameters. The detector layer is assumed to act as a thin scatterer, i.e. only the track angles are influenced. The expected variance of the scattering angles is calculated according to the known formula (3.3) derived from multiple scattering theory as defined in chapter 3. The momentum of the particle is calculated from the momentary track parameters. In addition, the thickness of the layer is adjusted to match the effective pathlength of the particle in the detector material. The relevant angles of incidence that are used to compute the pathlength are given by the track angles ϕ and λ at the hit position. Random scattering angles are then drawn from a normal

distribution with the calculated scattering angle variance and a mean of zero and added to the track angles. An illustration of this procedure is given in 6.1b.

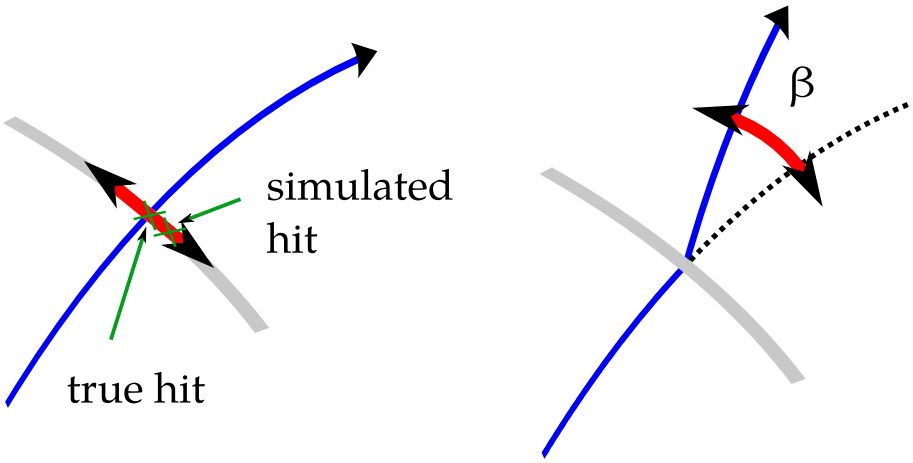

(a) Pixel Size (b) Multiple Scattering

Figure 6.1: The working principles of the uncertainty simulation for errors originating from the finite pixel size and from multiple scattering.

6.1.4 Pixel Size

The finite pixel size is simulated using gaussian smearing along the detector plane. At the true hit position, as determined by the track propagation described above, the detector plane is defined by two unit vectors. The first one is the unit vector $\hat{\boldsymbol{z}}$ along the z axis and the second one is the unit vector $\hat{\boldsymbol{\varphi}}$ along the φ direction in cylindrical coordinates. Pixel errors manifest only along these two directions. Assuming the hit position inside a real pixel to be uniformly distributed over its area, the variance in each pixel direction is defined as $\sigma^2 = \frac{1}{12}s^2$ with s being the pixel size along one dimension. To simulate the finite resolution of the hit position, random numbers are drawn from a normal distribution with the aforementioned

variance and added to the true hit position along the defined unit vector. This procedure is illustrated in 6.1a.

6.2 Reconstruction and Performance

Three different algorithms are used to reconstruct each track: the fast helix fit (*fast helix 1*), the fast helix fit with a single recalculation of the weights (*fast helix 2*) and the *broken lines* fit.

The fast helix fit is done according to the description in chapter 5. The weights are calculated using the simulated pixel size (the width of an equivalent normal distribution to be exact) of the detector. The reweighted fast helix is an iterative procedure with the first iteration being identical to the simple fast helix fit. Then, the incident angles of the track are calculated with respect to the detector layers using the results from the initial fit, and the initial weights are projected onto the planes perpendicular to the track. In the second iteration, these recalculated weights are used.

The broken lines fit is performed as described in section 5.4. The spatial weights are identical to the recalculated weights of the reweighted fast helix fit. To compute the weights for the kink angles, the expected scattering angle variance is calculated according to (3.3) using the track momentum from the initial helix fit and the thickness of the detector layers.

The quality of the fit is judged by two different quantities, the resolution and the error description. The resolution is examined using the parameter delta, i.e. the difference between the generated and the reconstructed parameter. For an example parameter α, the quantity $\Delta = \alpha_{truth} - \alpha_{reco}$ is plotted in a histogram. Under the assumption of normal measurement errors and linear error propagation from the measurements to the reconstructed parameters, Δ follows a normal distribution. The mean is zero for an unbiased estimation and a non-zero mean indicates a bias in the reconstruction algorithm. The width, i.e. the standard deviation, determines the parameter resolution. A small resolution value indicates that the estimated parameter describes the true track well. [1]

The error description can be checked by analyzing the so-called *pull* distribution. The pull of the reconstruction is the parameter delta divided by the standard deviation of the reconstructed parameter as given by the fit algorithm, e.g. $(\alpha_{truth} - \alpha_{reco})/\sigma_\alpha$. If the error description is correct, the

[1] This is only true if the distribution is normal. Otherwise a more robust estimator needs to be used.

scale of the parameter errors given by the fit coincides with the parameter resolution calculated using the parameters' delta distribution. In this case, the pull distribution is a standard normal distribution with a mean of zero and a standard deviation of 1. A pull width lower than 1 is evidence for an overestimation of the parameter error and a higher width indicates an underestimation.

6.3 Simple Geometry

Before investigating the fit performance with the MU3E baseline design, the fitness of my implementations will be tested. To this end, the fit performance for both algorithms is analyzed for a simplified detector using the aforementioned track generator with a fixed parameter set in the different tracking regimes described in section 5.1. The detector dimensions are similar to the baseline design, but with four equidistant layers instead of two double layers. The layers are equidistant cylinders with radii at 2 cm, 4 cm, 6 cm and 8 cm, with the overall dimensions similar to the baseline design in chapter 3. A sample of 1×10^5 tracks is generated using the fixed track generator with the following initial parameters:

$$(\kappa, \phi, \tan\lambda, d_{ca}, z_0)^T = (-7.0, \tfrac{1}{2}\pi, -0.3, 0.004, -0.02) \tag{6.1}$$

The reconstructed track parameters are always defined with respect to the first hit position. The results of the fit performance investigation are illustrated using the curvature parameter κ as an example. Similar arguments apply also for the other track parameters and the corresponding performance plots can be found in chapter B in the appendix.

6.3.1 Spatial Regime

As a consistency check, the performance of all fit algorithms is tested in the purely spatial tracking regime. During the simulation only the pixel size simulation with a pixel size of 100 µm is activated and no multiple scattering is considered. Therefore, the true track is an ideal helix and all reconstruction uncertainties should only originate from the uncorrelated spatial uncertainties. The weights for the fast helix fit are calculated from the simulated pixel size. For the broken lines fit, the spatial weights are identical to the ones used for the fast helix fits. Since no multiple scattering is simulated, the scattering angle variances are calculated using an

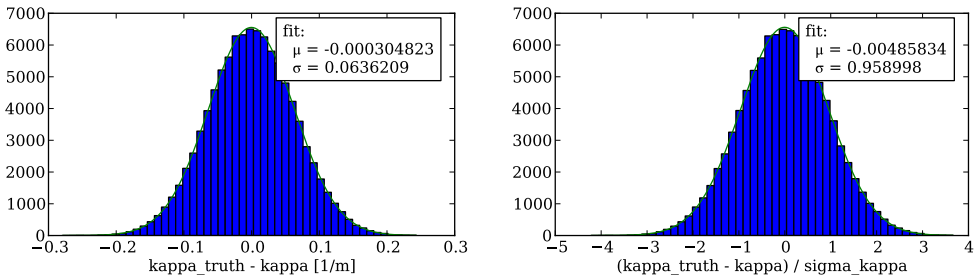

Figure 6.2: The fast helix fit κ delta and pull distributions in the spatial regime.

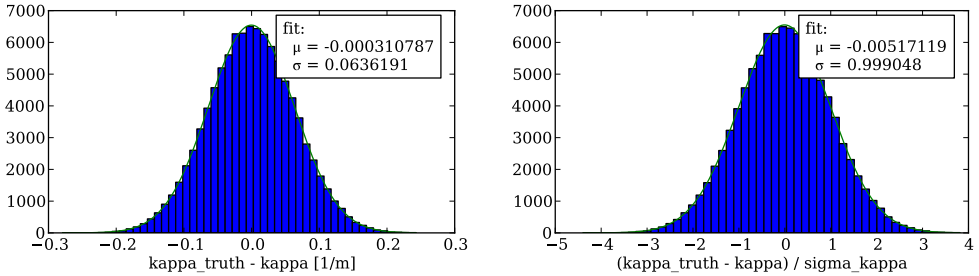

Figure 6.3: The reweighted fast helix fit κ delta and pull distributions in the spatial regime.

arbitrarily low material thickness of $1 \times 10^{-6} X_0$. In turn, the associated weights become accordingly large.

In Figure 6.2, Figure 6.3 and Figure 6.4 the resulting parameter delta and pull distributions are shown for the fast helix fit, the reweighted fast helix fit and the broken lines fit, respectively. The normal distribution for each dataset is plotted in green with the mean and the standard deviation calculated from the data. All distributions are well modeled by a normal distribution.

The distribution width for the parameter delta is almost identical for all fitting algorithms in the case of low κ. This is expected for the fast helix fits and confirms the working implementation of the broken lines fit. According to (5.13), increased scattering weights penalize any deviations from a vanishing scattering angle during reconstruction. The broken lines fit thus reduces to the initial fast helix fit. Besides, the distribution means are all very close to zero and indicate that none of the fitting algorithms are biased.

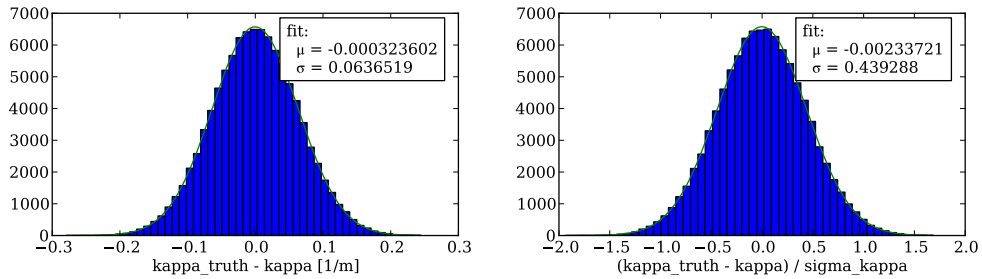

Figure 6.4: The broken lines fit κ delta and pull distributions in the spatial regime.

The pull distribution width for the fast helix fit is very close to one. The remaining deviations originate from the non-orthogonal angles of incidence at later detector layers. Hence, these deviations are eliminated in the reweighted fast helix fit. The broken lines pull width differs from the fast helix pull widths. Since the broken lines fit also includes the non-existing scattering angles, the error description contains extra terms that impair the result. This leads to an error overestimation and thus a pull distribution width smaller than one.

6.3.2 Scattering Regime

To inspect the effect of pure multiple scattering, the algorithms are also tested in a simulation without pixel errors. Here, the simulation uses a layer thickness of $0.001 X_0$ for the multiple scattering effects. The spatial weights are calculated using an arbitrarily small pixel size of 1×10^{-6} µm and the scattering weights use the simulated thickness.

The resulting delta and pull distributions are displayed in Figure 6.5, Figure 6.6 and Figure 6.7. The distributions are again well modeled by a Gaussian and the delta distributions show no sign of bias. Only the pull distribution for the broken lines fit seems to be slightly skewed. This is most likely a remnant of the choice of a fixed sign of the initial value of κ. The width of the delta distributions is now one order of magnitude higher than in the spatial regime ($\sigma_{spatial} \sim 0.064\,\mathrm{m}^{-1}$ vs. $\sigma_{scattering} \sim 0.25\,\mathrm{m}^{-1}$). This confirms that the scattering uncertainties are indeed dominating in this setup and manifest in the higher delta variance. However, the broken lines fit does not improve in resolution with respect to the fast helix fits. An explanation is given in detail in section 6.4.

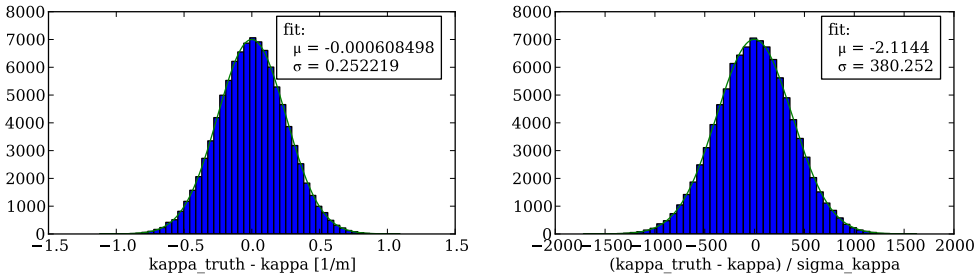

Figure 6.5: The fast helix fit κ delta and pull distributions in the scattering regime.

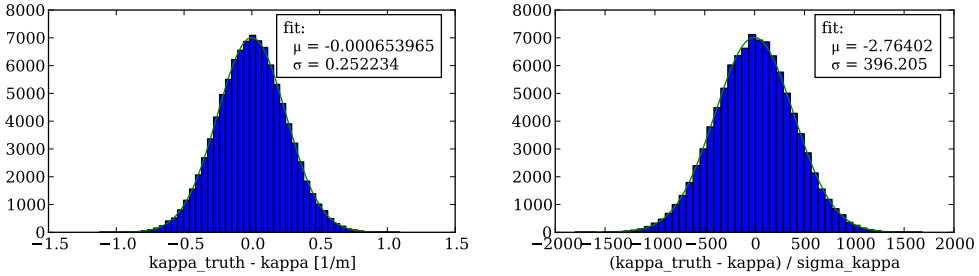

Figure 6.6: The reweighted fast helix fit κ delta and pull distributions in the scattering regime.

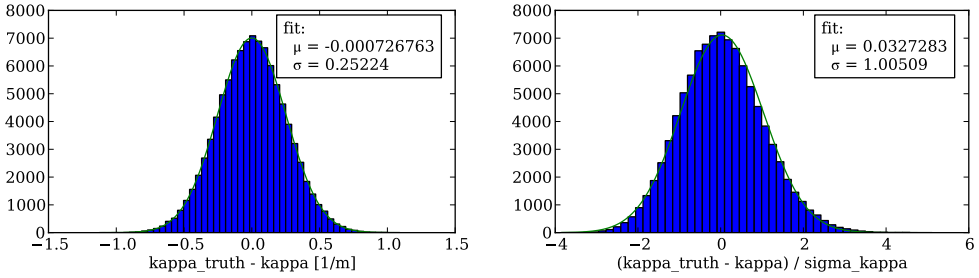

Figure 6.7: The broken lines fit κ delta and pull distributions in the scattering regime.

The pull widths for the fast helix fits are orders of magnitude off. This is not surprising since the influences from multiple scattering on the measurement variances are not considered. Only the broken lines fit provides a correct error description.

6.3.3 Full Range

To test the full parameter range, a sample of 1×10^5 tracks drawn from the full parameter range is used. The resulting resolutions depend on the initial particle momenta and are binned in κ. For each bin, the width of the delta and the pull distribution is calculated and shown. The displayed x-error corresponds to the bin width and the y-error reflects the statistical error of the distribution widths.

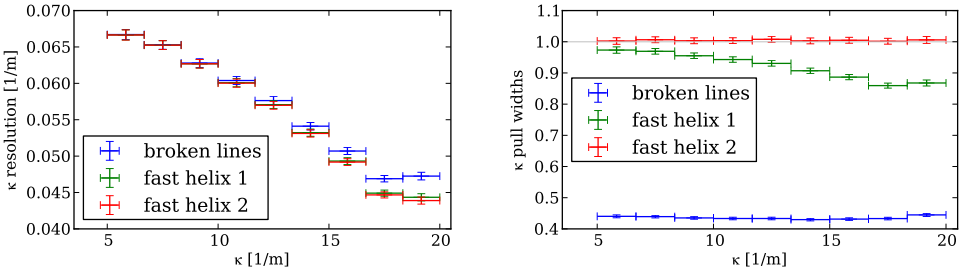

Figure 6.8: The κ resolution and pull distribution widths for all three fit algorithms in the spatial regime for the simplified geometry. The broken lines fit in the left plot is completely covered by the fast helix fit results.

In the case of the purely spatial regime, the resulting performance can be seen in Figure 6.8. The absolute κ resolution decreases with increasing κ for all algorithms. The fast helix fits have equal resolution and the broken lines fit resolution is slightly worse in the high κ regime. This is most probably an artifact of the chosen finite layer thickness that does not completely supress multiple scattering.

The pull widths differ for the three fit algorithms. The reweighted fast helix fit performs best and gives the correct error description over the full range. The regular fast helix fit slightly overestimates the errors. This effect is more pronounced for high curvatures where the angles of incidence are more inclined. The broken lines fit is constantly overestimating the errors due to the inclusion of the non-existing multiple scattering as described above.

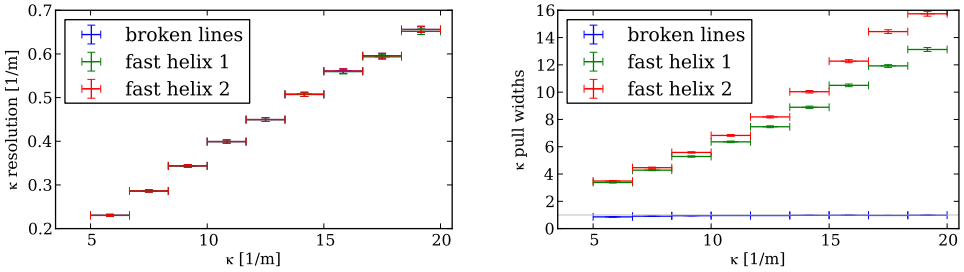

Figure 6.9: The κ resolution and pull distribution widths for all three fit algorithms in the scattering regime for the simplified geometry.

The fit performance in the scattering regime without pixel errors is shown in Figure 6.9. Here, the behavior is quite different from the spatial regime. The resolution increases with increasing κ for all fitting algorithms and only the broken lines fit provides a correct error description.

Simulating both pixel errors and multiple scattering results in similar performances as in the case with solely multiple scattering. The complete simulation will be explained in full detail when discussing the results for the MU3E baseline geometry.

6.4 Baseline Geometry

After showing that the implementations of the two fit algorithms work as expected, I will proceed to check their performance for the MU3E baseline geometry defined in chapter 3. The design in the simulation defines two double layers of sensors. The detector barrels of the first doublet are positioned at radii 1.58 cm and 2.41 cm and the second double layer is at radii 6.14 cm and 7.03 cm. These values correspond to the median radii of the physical sensor layers. The sensor pixels are assumed to be quadratic with a size of 100 µm in both directions. Multiple scattering is simulated at each detector layer assuming a thin scatterer with a thickness of 0.001 in units of the radiation length X_0. An exact knowledge of the composition of the layers in terms of specific materials is not required, since the simulation is not using a full scattering simulation. All tracks are generated in the transverse plane only, i.e. the parameters $\tan\lambda$ and z_0 are fixed to zero and the other parameters are drawn from a uniform distribution as defined above.

The chosen values for the pixel size and the detector thickness differ slightly from the proposed values defined in chapter 3. This is a deliberate choice. The simplified simulation is missing several effects that will exists in the real detector such as multiple scattering in the helium atmosphere or noise hits. Using higher values, e.g. for the detector thickness, can compensate for these missing effects. In addition, we are interested in the general feasibility of broken lines track fitting in the context of the MU3E experiment and not yet in the detailed description of the expected performance, e.g. as it would be required for a technical design report. Here, the absolute values for the achievable resolution are not as important as the differences between the fit algorithms. Therefore, the chosen detector parameters are reasonable estimates for the task at hand and should be fit to give insights into the possible performance improvements with the broken lines fit.

Again, the performance of the following three fit algorithms is compared: the plain fast helix fit (*fast helix 1*), the fast helix fit with a single additional iteration to correctly project the spatial uncertainties (*fast helix 2*) and the *broken lines* fit. In addition, I will focus on all the transverse parameters.

6.4.1 Parameter Resolution at the First Hit

Eventually, the parameter resolution needs to be determined at the vertex position of a possible signal decay. Since at this stage only single tracks are considered, no associated vertex position exists. Instead, an arbitrary reference point needs to be chosen. The natural reference points for the broken lines fit are the intersections of the reference track with the detector/scattering planes. Here, the intersection with the first detector layer is chosen. This position is closest to the target and should allow a precise propagation to a possible vertex position.

Figure 6.10 shows the fit performance for κ. The absolute resolution plot on the left side shows very little difference between the algorithms. The overall increasing difference between simulated and reconstructed parameter for higher κ is due to the increased effects from multiple scattering for lower momenta. The fact that all fits perform equally is unexpected in case of the broken lines fit. However, it can be explained by the definition of the correction to κ in the broken lines fit. $\Delta\kappa$ is a global correction that plays a role solely in the definition of the reconstructed kink angles.

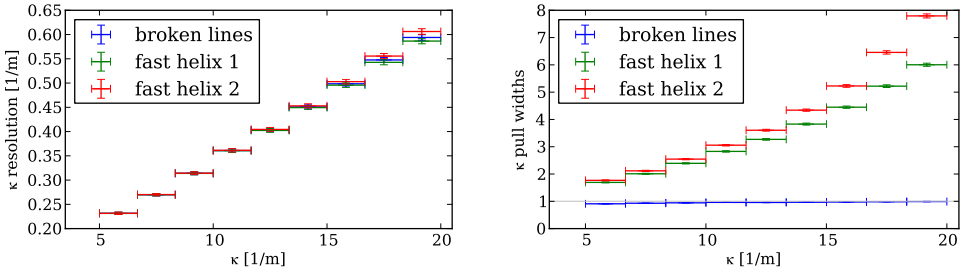

Figure 6.10: κ resolution and pulls for the baseline design. The reconstruction pivot is set to first hit position.

With just four layers, only two reconstructed kink angles are defined. This provides not enough constraints to enhance the kappa resolution.

In contrast to the resolution, the pull widths, shown in the right plot, differ amongst the algorithms. Both fast helix fits underestimate the errors with increasing margins as the effect of multiple scattering increases. This is expected since the fast helix fits do not take the additional measurement uncertainties due to multiple scattering into account. The broken lines fit does and provides a correct error estimate over the whole simulated κ range.

The reweighted fast helix fit performs worse than the regular one. In the second iteration, the variances for the later measurements are reduced to account for non-orthogonal angles of incidence. This is correct for tracking in the spatial regime. However, the scattering regime quite the opposite is true. The effect of multiple scattering on the expected measurement variance[2] is more pronounced for later measurements. Therefore, the variances should increase. The fact that the reweighted fast helix fit performs worst and the broken lines fit performs best in error description, indicates that the baseline design is dominated by multiple scattering uncertainties.

Figure 6.11 shows the resulting performance for the ϕ parameter. The resolution increases in general with increasing κ. Again, this can be attributed to the increasing effects of multiple scattering. In contrast to the κ case, the broken lines fit shows an improvement in resolution for ϕ. This improvement of up to approx. 20 % is more pronounced with higher κ. In the broken lines fit, the track angle at the first hit is not a global parameter anymore. It is essentially determined by the first two hit positions and

[2] In the case of a global circle/helix fit.

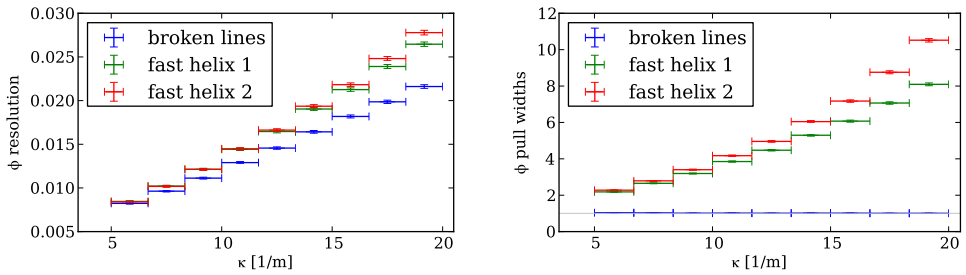

Figure 6.11: ϕ resolution and pulls for the baseline design. The reconstruction pivot is set to first hit position.

the influence from subsequent measurements is greatly diminished. The behavior of the error description is almost identical to the κ case, i.e. the broken lines fit describes them correctly and the fast helix fits does not, and the same explanation applies. Once more, the reweighted fast helix fit performs worst and the fast helix fit performs best, which can now be seen in the resolution as well.

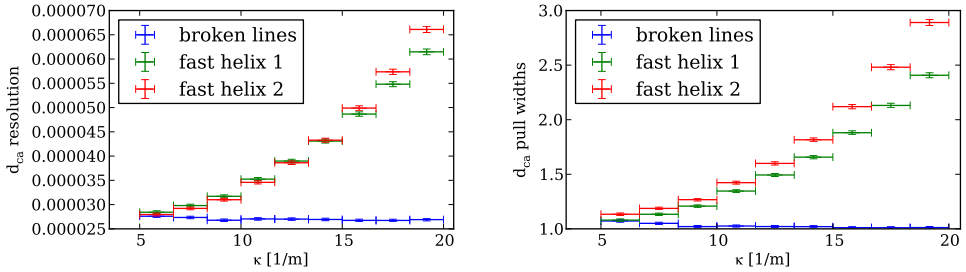

Figure 6.12: d_{ca} resolution and pulls for the baseline design. The reconstruction pivot is set to first hit position.

The performance for the d_{ca} parameter can be seen in Figure 6.12. This parameter exhibits a striking difference of up to approx. 50 % in resolution between the broken lines fit and the fast helix fits. The achievable resolution from the broken lines fit is almost constant over the whole κ range, whereas it increases with κ for the fast helix fits. For the broken lines fit, d_{ca} is a purely local parameter determined by the local offset u_i at the first hit position. It is influenced mostly by the pixel error and almost decoupled of multiple scattering effects. This is not the case for the fast helix fits where d_{ca} remains a global parameter influenced by multiple scattering. Similar

to the two previous parameters, the pull widths distribution is flat for the broken lines fit. However, the underestimation of the errors by the fast helix fits is less pronounced than in the two previous cases.

Overall, the broken lines fit performs best and the reweighted fast helix performs worst. This can be seen most clearly in the error description.

6.4.2 Parameter Resolution at the Origin

Based on the definition of the broken lines fit, estimating the parameters at the first hit is the best case scenario in terms of parameter resolution. At this position the track parameters have the least correlations. The offset measurements are mostly determined by the small pixel size and the reconstructed scattering angles are defined at the hit position itself. No additional transport of either the parameters or the covariance matrix is required.

In a more realistic reconstruction scenario, the parameters need to be reconstructed with respect to a possible vertex position and the parameters defined at the first hit need to be transported to the said vertex. The Jacobi matrix that defines the transformation is non-diagonal (see section 4.4). This immediately reintroduces correlations among the track parameters and increases the associated variances. To see how the fit algorithms fare in this case, the resolution and the pulls can also be calculated with respect to the origin. After the initial reconstruction, the parameter and their associated covariances are transported to the origin as a new reference point using the procedures defined in section 4.4.

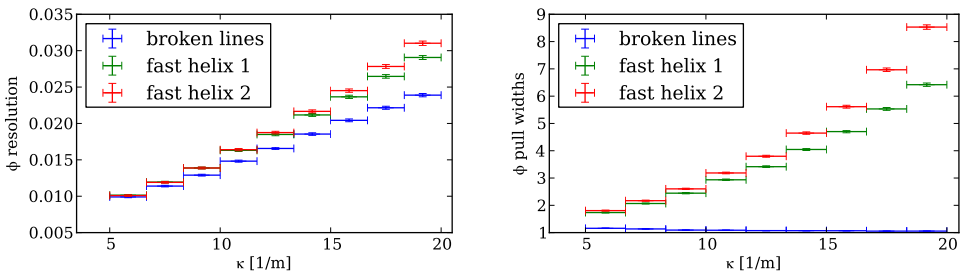

Figure 6.13: ϕ resolution and pulls for the baseline design. The parameters are reconstructed at the first hit position and then transported to the origin of the coordinate system.

The reconstruction performance for the ϕ parameter is shown in Figure 6.13. The overall qualitative picture is quite similar to the initial fit shown in Figure 6.11. The broken lines fit still gives a higher resolution but the absolute resolution is slightly increased. This is a result of the additional errors acquired in the covariance transformation. However, the error description is still correct for the broken lines fit which implies that the linear error propagation is sufficient.

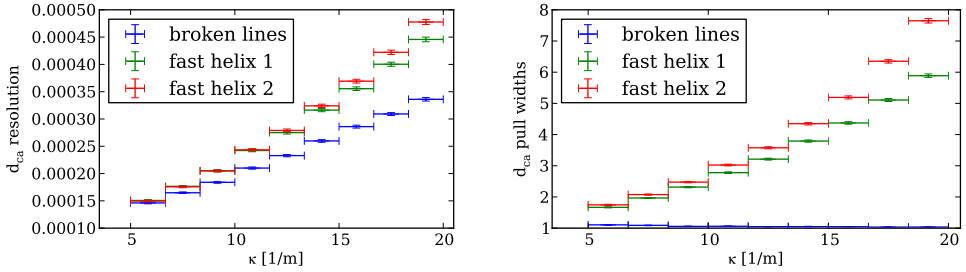

Figure 6.14: d_{ca} resolution and pulls for the baseline design.The parameters are reconstructed at the first hit position and then transported to the origin of the coordinate system.

Figure 6.14 shows the transported performance plots for d_{ca}. Here, the change with respect to the untransported case in Figure 6.12 is dramatic. In the former case, the resolution was almost flat for the broken lines fit whereas in this case the uncertainty increases for higher κ. At the hit position the d_{ca} measurement is almost independent of the scattering angles, but the following transport depends heavily on the track angle and its uncertainty. Since the angle uncertainty is dominated by the multiple scattering uncertainty that depends in turn on the momentum, a decrease in resolution is seen for lower momentum, i.e. higher values of κ. However, the quality of the error description persists.

A plot for κ is not shown because it is invariant under changes of the reference point. Hence, the performance of the κ fit is independent of the reference point.

6.4.3 Momentum Resolution

As shown in section 4.5, the transverse momentum p_T depends only on the measurement of the curvature κ as $p_T = \frac{qB}{c\kappa}$ and can be calculated using the known (simulated) value of the magnetic field. The resulting absolute

resolution for the transverse momentum is shown in Figure 6.15. Similar

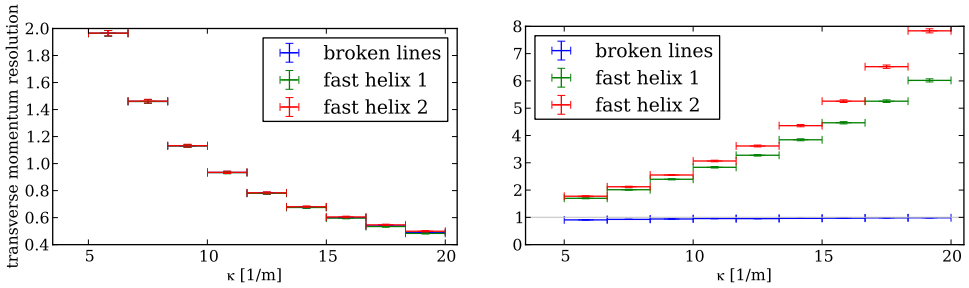

Figure 6.15: Transverse momentum resolution and pulls as a function of κ. The tracks were simulated using the baseline design.

to the κ resolution, the broken lines fit does not improve with respect to the fast helix fit. The error on p_t can be calculated from Equation 4.26 using error propagation and the resulting pull plots in Figure 6.15 show the correct error description for the broken lines fit.

The total momentum resolution also depends on the track angle λ in the longitudinal plane. Although not presented here, the expected performance can be estimated from the performance of the broken lines fit in the transverse plane. Since the broken lines fit for straight tracks, i.e. the particle motion in the longitudinal plane, is almost identical to the one for the curved tracks, a similar behavior for the track angle resolution can be expected. This would entail a resolution increase for λ and, as a consequence, a resolution increase for the total momentum resolution. The size of this expected effect and its dependence on κ and λ still need to be determined.

6.5 Summary

The initial tests of the fit algorithms show that the implementations generally work as expected. The fast helix fit performs poorly in the presence of multiple scattering. Its error description is incorrect since the increased measurement variances due to multiple scattering are not taken into account. The broken lines fit shows potential for the utilization in the MU3E experiment, although the missing improvements in terms of κ resolution are less than what was hoped for. Nevertheless, the error description of the broken lines fit is correct. Overall, it is clear that the MU3E tracking

measurements are dominated by multiple scattering and that the effects due to the finite pixel size are almost negligible.

Chapter 7

Discussion and Outlook

The MU3E experiment is a proposed precision experiment to search for the lepton flavor violating decay $\mu^+ \to e^+e^+e^-$. The sensitivity goal is to measure a branching ratio of BR($\mu^+ \to e^+e^+e^-$) < 1×10^{-16}, four orders of magnitude below the current experimental limit [Sch+12]. Many theories for physics beyond the Standard Model predict branching ratios higher than the proposed sensitivity and below the current experimental limit of BR($\mu^+ \to e^+e^+e^-$) < 1×10^{-12}. This high precision measurement would allow a search for new physics at a mass scale beyond what is currently achievable with direct searches.

To reach the proposed sensitivity a very high reduction of possible backgrounds is necessary. This entails the need for an extremely precise measurement of the decay electrons. These electrons have only little momentum bound by half the muon mass or approx. 53 MeV/c. Thus, multiple scattering effects are the dominating source of measurement uncertainties.

The MU3E detector is a magnetic spectrometer optimized to measure the low momentum electrons. It consists of four cylindrical layers of thin silicon pixel sensors in a strong solenoidal magnetic field. The low number of sensor layers and its small total material budget are designed to minimize multiple scattering effects. Since the electrons are charged particles, they move in the solenoidal field along a helix with a curvature dependent on the particle momentum.

In addition to the required resolution, a high number of stopped muons and their decays need to be analyzed. This requires a high intensity primary beam. Ultimately, the MU3E experiment intends to use a muon beam with a muon rate of up to $2 \times 10^9\,\mathrm{s}^{-1}$.

Track reconstruction algorithms for this experiment need to be able to both allow a high precision in the presence of high multiple scattering and they need to be fast enough to allow the reconstruction of all the possible decay tracks. In this thesis, a novel track fitting algorithm based on broken lines was investigated that takes multiple scattering into account explicitly [Blo06]. The broken lines fit results were compared with those of a simple fast helix fit. All studies were performed for the track parameters describing the motion in the transverse plane.

The fast helix fit is a global least squares fit. It uses the ideal track model of a helical motion and directly fits it to the measured positions. Each measurement is weighted according to the pixel resolution. The broken lines fit is a detailed refit of the residuals from a preceding fast helix fit. In the residual system, a linearized track model can be used. Scattering angles are explicitly taken into account using the local offsets and the kink angles calculated from neighboring positions. The local offsets are weighted according to the pixel resolution and the kink angle weights result from multiple scattering theory.

The fast helix fit performs poorly in the presence of multiple scattering. The error description used for this simple fast helix fit is incorrect since the additional measurement variances due to multiple scattering are not taken into account. All estimated parameters depend on all measurements and are consequently influenced by the correlations induced by multiple scattering.

The broken lines fit shows improvements in parameter resolution with respect to the fast helix fit depending on the locality of the estimated quantity. No improvement is seen for the curvature κ as it is a global parameter in both the fast helix and the broken lines fit and always depends on all measured positions. The initial track angle ϕ shows slight improvements of up to 20 % at the maximum simulated curvature. In the broken lines fit, ϕ depends only on the first two measurements and is less influenced by the correlations between later hit positions. The biggest improvement can be seen for the distance of closest approach d_{ca}, with a better parameter description of up to 50 %. It is a purely local parameter and its accuracy in the broken lines scheme depends almost only on the pixel resolution. In addition to the improved parameter resolution, the broken lines fit describes the resulting parameter uncertainties correctly.

An extension to the fast helix fit that uses recalculated weights was also investigated, but its performance was identical or worse in comparison to the regular fast helix fit.

These studies show that for the correct track reconstruction in the MU3E experiment a correct consideration of multiple scattering is crucial. Here, the broken lines fit was chosen to treat multiple scattering effects in the track reconstruction. However, most current particle physics experiments employ iterative track fitting procedures based on the Kálmán-filter to handle multiple scattering [Fru87]. A comparison of the Kálmán-filter approach and the broken lines fit was not part of this thesis.

It can be shown that the Kálmán-filter method and the generalized broken lines fit in three dimensions are mathematically equivalent [Kle12]. Both algorithms are expected to lead to a similar parameter resolution. However, the former method is an iterative procedure and the latter one is a non-iterative direct one. Depending on the geometry and the reconstruction strategy, one of the two methods will be preferred in terms of computing time. A detailed study of the possible performance differences in the context of the MU3E experiment remains to be done.

The broken lines fit that was tested here is a two dimensional fit in the transverse plane. This means that possible correlations between the transverse and the longitudinal plane are ignored. As mentioned above, it is possible to generalize the broken lines fit to three dimensions [Kle12]. A comprehensive analysis of possible improvements with respect to the two dimensional case would be one of the next steps to consider.

In this study, only single tracks were investigated and a simple simulation was used. For the real experimental situation multiple tracks need to be reconstructed and common vertices of multiple tracks need to be reliably determined. The correct error description of the track parameters, as shown in this study for the broken lines fit in the transverse plane, is a prerequisite for any possible vertex fit. In addition, a full detector simulation is necessary to allow the selection of a suitable track fitting algorithm under more realistic conditions.

Appendix A

Derivations

A.1 Helical Tracks

A.1.1 Karimaeki Parametrization

The derivation of the required substitutions to describe the track as a function of the transverse arc length:

$$
\begin{aligned}
da^2 &= dx^2 + dy^2 && \text{(A.1)}\\
&= ds^2 - dz^2 && \text{(A.2)}\\
\implies \frac{da}{ds} &= \sqrt{1 - (\hat{\boldsymbol{t}} \cdot \hat{\boldsymbol{z}})^2} && \text{(A.3)}\\
&= \sqrt{1 - \gamma^2} && \text{(A.4)}\\
\frac{\alpha}{\sqrt{1-\gamma^2}} &= \frac{\left\|\hat{\boldsymbol{t}}_0 \times \hat{\boldsymbol{z}}\right\|}{\sqrt{1 - (\hat{\boldsymbol{t}}_0 \cdot \hat{\boldsymbol{z}})^2}} && \text{(A.5)}\\
&= \frac{\left\|\hat{\boldsymbol{t}}_0\right\| \|\hat{\boldsymbol{z}}\| \sin\delta}{\sqrt{1 - (\left\|\hat{\boldsymbol{t}}_0\right\| \|\hat{\boldsymbol{z}}\| \cos\delta)^2}} && \text{(A.6)}\\
&= \frac{\sin\delta}{\sqrt{1 - \cos\delta^2}} && \text{(A.7)}\\
&= 1 && \text{(A.8)}\\
\theta &= Qs && \text{(A.9)}\\
&= -\frac{\alpha}{\sqrt{1-\gamma^2}} \kappa a && \text{(A.10)}\\
&= -\kappa a && \text{(A.11)}
\end{aligned}
$$

A.1.2 Covariance Transformation

The Jacobi matrix required for the transformation of the covariance matrix is given by

$$J = \begin{pmatrix} 1 & 0 & 0 & 0 & 0 \\ \xi\Delta_{\parallel} & \xi u\nu & -\xi\kappa^2\Delta_{\parallel} & 0 & 0 \\ \mu\zeta - \tau A & 2\mu u\Delta_{\parallel} & 2\mu\nu & 0 & 0 \\ 0 & 0 & 0 & 1 & 0 \\ \omega(\frac{1}{\kappa}\phi' - \xi\Delta_{\parallel}) & \omega(1-\xi\mu\nu) & \omega\xi\kappa^2\Delta_{\parallel} & (\phi-\phi')/\kappa & 1 \end{pmatrix} \tag{A.12}$$

with the following additional constants [Kar91; Gro97]:

$$\begin{aligned} \nu &= 1 + \kappa\Delta_{\perp} \\ \xi &= \left(B^2 + C^2\right)^{-1} \\ \tau &= \tfrac{1}{2}A\left((1+U)^2U\right)^{-1} \\ \mu &= \left(U(1+U)\right)^{-1} + \kappa\tau \\ \zeta &= \Delta_{\perp}^2 + \Delta_{\parallel}^2 \\ \omega &= \tan\lambda/\kappa \end{aligned} \tag{A.13}$$

A.2 Track Fitting

A.2.1 Linear Least Squares Normal Equations

$$\begin{aligned} \frac{\partial S}{\partial \alpha_k} &= 2\sum_{i=1}^{N}\left(y_i - \sum_{j=1}^{M} F_{ij}\alpha_j\right)(-F_{ik}) \\ &= 2\sum_{i=1}^{N}\sum_{j=1}^{M} F_{ik}F_{ij}\alpha_j - 2\sum_{i=1}^{N} F_{ik}y_i \\ &= 2\sum_{i=1}^{N}\sum_{j=1}^{M} F_{ki}^T F_{ij}\alpha_j - 2\sum_{i=1}^{N} F_{ki}^T y_i = 0 \end{aligned} \tag{A.14}$$

A.2.2 Linear Least Squares Parameter Covariance

For linear function of the form $\boldsymbol{y} = F\boldsymbol{x}$ and a know covariance matrix Σ for the values of x, propagation of uncertainties yields the covariance matrix

for the values of y as follows:

$$\Sigma = F\,\Sigma\,F^T \tag{A.15}$$

The optimal parameter values are linear functions of the measurements in the following form:

$$\boldsymbol{\alpha} = (F^T W F)^{-1} F^T W\,\boldsymbol{y} \tag{A.16}$$

Using the propagation of uncertainties as defined above and utilizing the relations $W = \Sigma_y$ as well as $W^T = W$, which is due to the diagonality of W, the parameter covariance matrix can be easily calculated.

$$\begin{aligned}\Sigma_\alpha &= \left(F^T W F\right)^{-1} F^T W \Sigma_y W^T F \left(F^T W F\right)^{-1} \\ &= \left(F^T W F\right)^{-1} F^T W F \left(F^T W F\right)^{-1} \\ &= \left(F^T W F\right)^{-1}\end{aligned} \tag{A.17}$$

Appendix B

Performance Plots

B.1 Spatial Regime

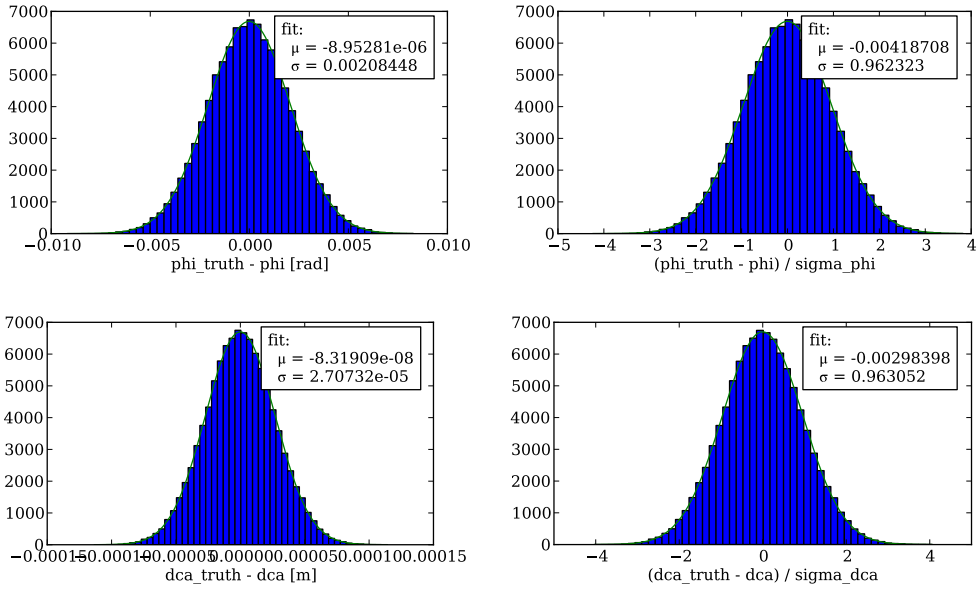

Figure B.1: The fast helix fit parameter delta and pull distributions for the additional parameters in the transverse plane in the spatial regime.

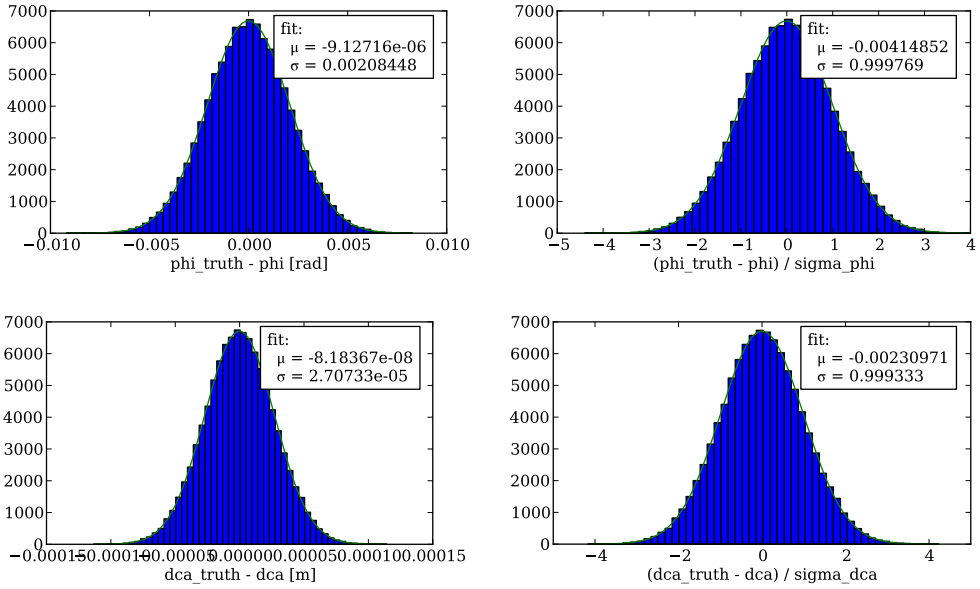

Figure B.2: The reweighted fast helix fit parameter delta and pull distributions for the additional parameters in the transverse plane in the spatial regime.

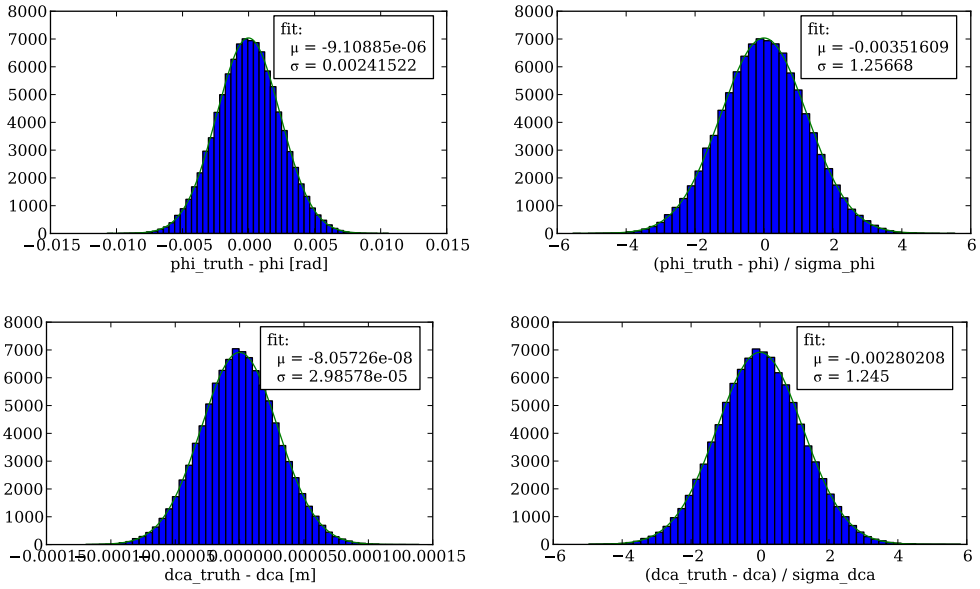

Figure B.3: The broken lines fit parameter delta and pull distributions for the additional parameters in the transverse plane in the spatial regime.

B.2 Scattering Regime

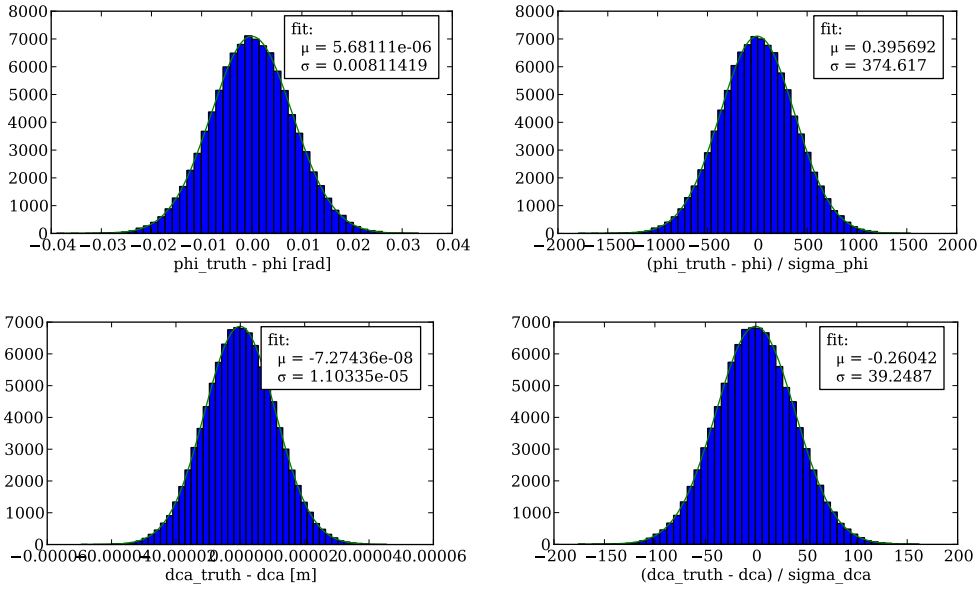

Figure B.4: The additional transverse fast helix fit parameter delta and pull distributions in the scattering regime.

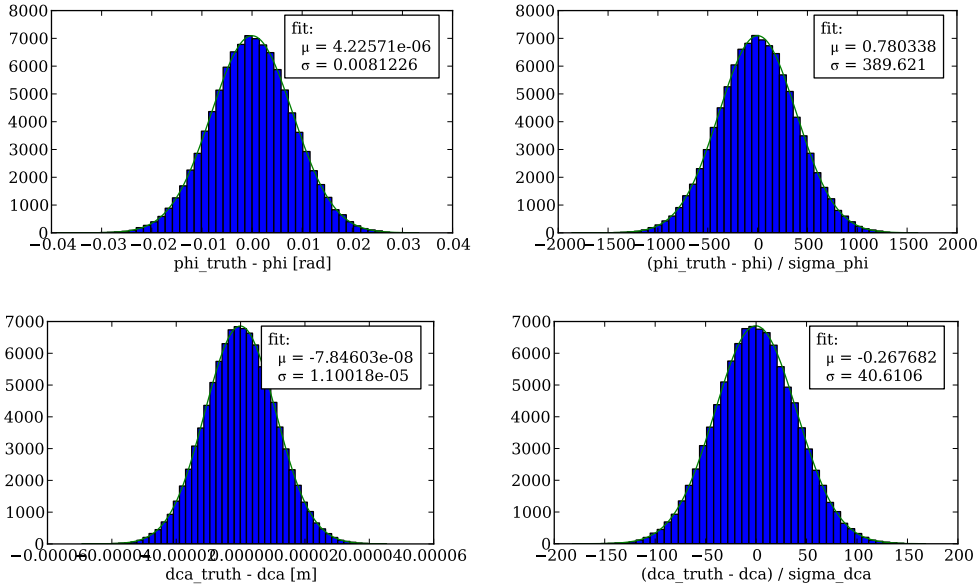

Figure B.5: The additional transverse reweighted fast helix fit parameter delta and pull distributions in the scattering regime.

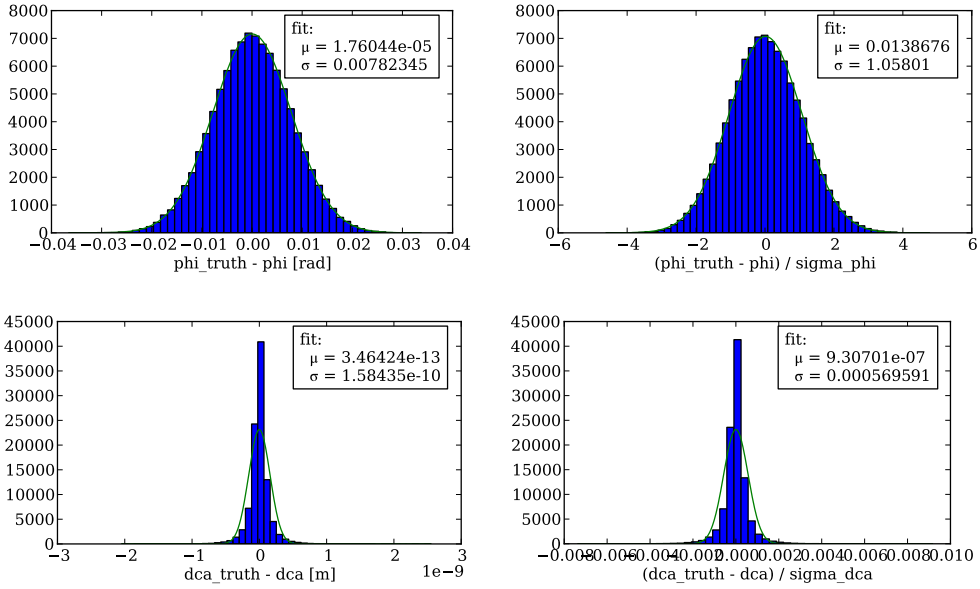

Figure B.6: The additional transverse broken lines fit parameter delta and pull distributions in the scattering regime.

Bibliography

[Aad+11a] Georges Aad et al. "Limits on the production of the Standard Model Higgs Boson in pp collisions at sqrt(s) =7 TeV with the ATLAS detector". In: *Eur.Phys.J.* C71 (2011), p. 1728. DOI: 10.1140/epjc/s10052-011-1728-9. arXiv:1106.2748 [hep-ex].

[Aad+11b] Georges Aad et al. "Searches for supersymmetry with the ATLAS detector using final states with two leptons and missing transverse momentum in $\sqrt{s}$ = 7 TeV proton-proton collisions". In: (2011). arXiv:1110.6189 [hep-ex].

[Aad+11c] Georges Aad et al. "Search for Diphoton Events with Large Missing Transverse Momentum in 1 fb^{-1} of 7 TeV Proton-Proton Collision Data with the ATLAS Detector". In: (2011). arXiv:1111.4116 [hep-ex].

[Ada+11a] J. Adam et al. "New limit on the lepton-flavour violating decay $\mu^+ \to e^+\gamma$". In: *Phys.Rev.Lett.* 107 (2011), p. 171801. DOI: 10.1103/PhysRevLett.107.171801. arXiv:1107.5547 [hep-ex].

[Ada+11b] J. Adam et al. "New Limit on the Lepton-Flavor-Violating Decay $\mu^+ \to e^+\gamma$". In: *Phys. Rev. Lett.* 107 (17 Oct. 2011), p. 171801. DOI: 10.1103/PhysRevLett.107.171801.

[Ago+03] S. Agostinelli et al. "Geant4 — a simulation toolkit". In: *Nuclear Instruments and Methods in Physics Research Section A: Accelerators, Spectrometers, Detectors and Associated Equipment* 506.3 (2003), pp. 250 –303. ISSN: 0168-9002. DOI: 10.1016/S0168-9002(03)01368-8.

[Ahm+01] Q. R. Ahmad et al. "Measurement of the charged current interactions produced by B-8 solar neutrinos at the Sudbury Neutrino Observatory". In: *Phys. Rev. Lett.* 87 (2001), p. 071301. eprint: nucl-ex/0106015.

[Bay+11] R. Bayes et al. "Experimental Constraints on Left-Right Symmetric Models from Muon Decay". In: *Phys. Rev. Lett.* 106 (4 Jan. 2011), p. 041804. DOI: 10.1103/PhysRevLett.106.041804.

[Bel+88] U. Bellgardt et al. "Search for the Decay $\mu^+ \longrightarrow e^+e^+e^-$". In: *Nucl.Phys.* B299 (1988), p. 1. DOI: 10.1016/0550-3213(88)90462-2.

[Ber11] Niklaus Berger. "A Novel experiment searching for the lepton flavour violating decay $\mu \to eee$". In: *NUFACT 11, XIIIth International Workshop on Neutrino Factories, Super beams and Beta beams*. 2011. arXiv:1110.1504 [hep-ex].

[Bla+07] Monika Blanke et al. "Charged Lepton Flavour Violation and (g-2)(mu) in the Littlest Higgs Model with T-Parity: A Clear Distinction from Supersymmetry". In: *JHEP* 0705 (2007), p. 013. DOI: 10.1088/1126-6708/2007/05/013. arXiv:hep-ph/0702136 [hep-ph].

[Blo06] V. Blobel. "A new fast track-fit algorithm based on broken lines". In: *Nuclear Instruments and Methods in Physics Research Section A: Accelerators, Spectrometers, Detectors and Associated Equipment* 566 (2006), pp. 14–17.

[CMS11] CMS Collaboration. "Combination of SM Higgs Searches". In: CMS-PAS-HIG-11-032 (2011).

[CN05] We-Fu Chang and John N. Ng. "Lepton flavor violation in extra dimension models". In: *Phys.Rev.* D71 (2005), p. 053003. DOI: 10.1103/PhysRevD.71.053003. arXiv:hep-ph/0501161 [hep-ph].

[Cow04] Glen Cowan. *Statistical data analysis. [with applications from particle physics]*. eng. Repr. Oxford science publications. Oxford: Clarendon Press, 2004, XIV, 197 S. ISBN: 0-19-850156-0 ; 978-0-19-850156-5.

[Dem04] Wolfgang Demtröder. *Elektrizität und Optik. mit 17 Tabellen, zahlreichen durchgerechneten Beispielen und 143 Übungsaufgaben mit ausführlichen Lösungen*. ger. 3., überarb. u. erw. Aufl. Vol. 2. Experimentalphysik. Berlin ; Heidelberg [u.a.]: Springer, 2004, XIX, 482 S. ISBN: 3-540-20210-2 ; 978-3-540-20210-3.

[DK09] Rashid M. Djilkibaev and Rostislav V. Konoplich. "Rare Muon Decay $\mu^+ \to e^+e^-e^+\nu_e\bar{\nu}_\mu$". In: *Phys.Rev.* D79 (2009), p. 073004. DOI: 10.1103/PhysRevD.79.073004. arXiv:0812.1355 [hep-ph].

[EB64] F. Englert and R. Brout. "Broken Symmetry and the Mass of Gauge Vector Mesons". In: *Phys. Rev. Lett.* 13 (9 Aug. 1964), pp. 321–323. DOI: 10.1103/PhysRevLett.13.321.

[Egu+03] K. Eguchi et al. "First results from KamLAND: Evidence for reactor anti- neutrino disappearance". In: *Phys. Rev. Lett.* 90 (2003), p. 021802. eprint: hep-ex/0212021.

[Fou] Python Software Foundation. *The Python Programming Language*. URL: python.org (visited on 01/28/2012).

[FR00] R. Frühwirth and M. Regler. *Data analysis techniques for high-energy physics*. Ed. by R. Frühwirth and M. Regler. 2nd ed. Vol. 11. Cambridge monographs on particle physics, nuclear physics, and cosmology. Cambridge University Press, 2000.

[Fru87] R. Frühwirth. "Application of Kalman Filtering to Track and Vertex Fitting". In: *Nuclear Instruments and Methods in Physics Research A* 262 (1987), pp. 444–450.

[Fuk+98] Y. Fukuda et al. "Evidence for oscillation of atmospheric neutrinos". In: *Phys. Rev. Lett.* 81 (1998), pp. 1562–1567. eprint: hep-ex/9807003.

[GHK64] G. S. Guralnik, C. R. Hagen, and T. W. B. Kibble. "Global Conservation Laws and Massless Particles". In: *Phys. Rev. Lett.* 13 (20 Nov. 1964), pp. 585–587. DOI: 10.1103/PhysRevLett.13.585.

[Gro97] JLC Physics Group. *Introduction to Helical Track Manipulations*. Tech. rep. KEK, 1997.

[Hig64] Peter W. Higgs. "Broken Symmetries and the Masses of Gauge Bosons". In: *Phys. Rev. Lett.* 13 (16 Oct. 1964), pp. 508–509. DOI: 10.1103/PhysRevLett.13.508.

[HK85] H. E. Haber and G. L. Kane. "The Search for Supersymmetry: Probing Physics Beyond the Standard Model". In: *Phys. Rept.* 117 (1985), p. 75.

[J+–] Eric Jones, Travis Oliphant, Pearu Peterson, et al. *SciPy: Open source scientific tools for Python*. 2001–. URL: http://www.scipy.org/ (visited on 01/28/2012).

[Kar91] V. Karimäki. "Effective circle fitting for particle trajectories". In: *Nuclear Instruments and Methods in Physics Research Section A: Accelerators, Spectrometers, Detectors and Associated Equipment* 305 (1991), pp. 187–191.

[Kle12] Claus Kleinwort. "General broken lines as advanced track fitting method". In: *Nuclear Instruments and Methods in Physics Research Section A: Accelerators, Spectrometers, Detectors and Associated Equipment* (2012). ISSN: 0168-9002. DOI: 10.1016/j.nima.2012.01.024.

[KO01] Y. Kuno and Y. Okada. "Muon decay and physics beyond the standard model". In: *Rev. Mod. Phys.* 73 (2001), pp. 151–202. eprint: hep-ph/9909265.

[KOS03] M. Kakizaki, Y. Ogura, and F. Shima. "Lepton flavor violation in the triplet Higgs model". In: *Phys.Lett.* B566 (2003), pp. 210–216. DOI: 10.1016/S0370-2693(03)00833-5. arXiv:hep-ph/0304254 [hep-ph].

[LAP] LAPACK Contributors. *LAPACK — Linear Algebra PACKage*.

[MNS62] Ziro Maki, Masami Nakagawa, and Shoichi Sakata. "Remarks on the Unified Model of Elementary Particles". In: *Progress of Theoretical Physics* 28.5 (1962), pp. 870–880. DOI: 10.1143/PTP.28.870.

[Nak+10] K. Nakamura et al. "The Review of Particle Physics. Particle Data Group". In: *Journal of Physics G: Nuclear and Particle Physics* 37.075021 (2010).

[Noe18] Emmy Noether. "Invariante Variationsprobleme". In: *Nachr. D. König. Gesellsch. D. Wiss. Zu Göttingen* Math-phys. Klasse.1918 (1918), pp. 235–257.

[Per00] Donald H. Perkins. *Introduction to high energy physics*. eng. 4. ed., 1. publ. Cambridge [u.a.]: Cambridge Univ. Press, 2000, XIII, 426 S. ISBN: 0-521-62196-8 ; 978-0-521-62196-0.

[Per07] I. Peric. "A novel monolithic pixelated particle detector implemented in high-voltage CMOS technology". In: *Nucl.Instrum.Meth.* A582 (2007), pp. 876–885. DOI: 10.1016/j.nima.2007.07.115.

[PKF10] I. Peric, C. Kreidl, and P. Fischer. "Particle pixel detectors in high-voltage CMOS technology–New achievements". In: *Nucl. Instrum. Meth. A* In Press, Corrected Proof (2010), ISSN: 0168-9002. DOI: DOI:10.1016/j.nima.2010.11.090.

[Pre92] William H. Press, ed. *Numerical recipes in C. the art of scientific computing*. 2nd ed. Cambridge University Press, 1992.

[PT10] I. Peric and C. Takacs. "Large monolithic particle pixel-detector in high-voltage CMOS technology". In: *Nucl. Instrum. Meth.* A624.2 (2010). New Developments in Radiation Detectors - "Proceedings of the 11th European Symposium on Semiconductor Detectors, 11th European Symposium on Semiconductor Detectors", pp. 504 –508. ISSN: 0168-9002. DOI: DOI:10.1016/j.nima.2010.03.161.

[Sch+12] A. Schöning et al. "Letter of Intent for an Experiment to Search for the Decay $\mu \to eee$". Submitted to PSI Research Council. Jan. 2012.

[SW06] A. Strandlie and W. Wittek. "Derivation of Jacobians for the propagation of covariance matrices of track parameters in homogeneous magnetic fields". In: *Nuclear Instruments and Methods in Physics Research Section A: Accelerators, Spectrometers, Detectors and Associated Equipment* 566 (2006), pp. 687–698.

[Wik] Wikipedia Contributors. *Standard Model of Elementary Particles — Wikipedia, The Free Encyclopedia*.

Acknowledgements

An dieser Stelle möchte ich mich bei allen bedanken, die mich während meines Studiums und bei der Entstehung dieser Diplomarbeit unterstützt haben.

Zuerst möchte ich mich bei Prof. André Schöning bedanken, der mich auf das spannende Thema des MU3E Experiments aufmerksam gemacht hat und mich während meiner Arbeit hervorragend betreut hat.

Außerdem gilt mein Dank Prof. Ulrich Uwer, der sich sofort bereit erklärt hat diese Arbeit als Zweitgutachter zu beurteilen.

Ein besonderer Dank gilt außerdem Niklaus Berger und Dirk Wiedner, die mir während meiner Diplomarbeit jederzeit zur Verfügung standen, um Problem zu diskutieren und mir dadurch sehr weitergeholfen habe. Niklaus Berger gilt ein zusätzlicher Dank für die intensive Betreuung während der Schreibphase.

Bei allen Mitgliedern und Ehemaligen der Arbeitsgruppe André Schöning für die hervorragende Arbeitsatmosphäre und die unterhaltsame Ablenkung während nicht produktiver Phasen.

Ein großes Dankeschön gebührt natürlich meinen Freunden, die mir in meinem Studium immer zur Seite gestanden sind.

Zuletzt möchte ich mich Kristin Grußmayer und bei meiner Familie für die ihre Unterstützung bedanken. Diese Arbeit wäre ohne sie nicht möglich gewesen.

Erklärung:

Ich versichere, dass ich diese Arbeit selbstständig verfasst habe und keine anderen als die angegebenen Quellen und Hilfsmittel benutzt habe.

Heidelberg, den 1. Februar 2012 .....

Moritz Simon Maria Kiehn